The Astrophysical Journal, 915:35 (23pp), 2021 July 1 https://doi.org/10.3847/1538-4357/abfe0a

SDSS-IV MaNGA: Refining Strong Line Diagnostic Classifications Using Spatially Resolved Gas Dynamics

David R. Law[1], Xihan Ji[2], Francesco Belfiore[3], Matthew A. Bershady[4,5,6], Michele Cappellari[7], Kyle B. Westfall[8], Renbin Yan[2], Dmitry Bizyaev[9,10], Joel R. Brownstein[11], Niv Drory[12], and Brett H. Andrews[13]
[1] Space Telescope Science Institute, 3700 San Martin Drive, Baltimore, MD 21218, USA; dlaw@stsci.edu
[2] Department of Physics and Astronomy, University of Kentucky, 505 Rose Street, Lexington, KY 40506-0057, USA
[3] INAF—Osservatorio Astrofisico di Arcetri, Largo E. Fermi 5, I-50157, Firenze, Italy
[4] University of Wisconsin—Madison, Department of Astronomy, 475 N. Charter Street, Madison, WI 53706-1582, USA
[5] South African Astronomical Observatory, P.O. Box 9, Observatory 7935, Cape Town, South Africa
[6] Department of Astronomy, University of Cape Town, Private Bag X3, Rondebosch 7701, South Africa
[7] Sub-department of Astrophysics, Department of Physics, University of Oxford, Denys Wilkinson Building, Keble Road, Oxford OX1 3RH, UK
[8] University of California Observatories, University of California, Santa Cruz, 1156 High St., Santa Cruz, CA 95064, USA
[9] Apache Point Observatory and New Mexico State University, P.O. Box 59, Sunspot, NM, 88349-0059, USA
[10] Sternberg Astronomical Institute, Moscow State University, Moscow, Russia
[11] University of Utah, Department of Physics and Astronomy, 115 S. 1400 E., Salt Lake City, UT 84112, USA
[12] McDonald Observatory, The University of Texas at Austin, 2515 Speedway, Stop C1402, Austin, TX 78712, USA
[13] PITT PACC, Department of Physics and Astronomy, University of Pittsburgh, Pittsburgh, PA 15260, USA
Received 2020 November 10; revised 2021 April 23; accepted 2021 May 3; published 2021 July 1

Abstract

We use the statistical power of the MaNGA integral-field spectroscopic galaxy survey to improve the definition of strong line diagnostic boundaries used to classify gas ionization properties in galaxies. We detect line emission from 3.6 million spaxels distributed across 7400 individual galaxies spanning a wide range of stellar masses, star formation rates, and morphological types, and find that the gas-phase velocity dispersion $\sigma_{\mathrm{H}\alpha}$ correlates strongly with traditional optical emission-line ratios such as [S II]/Hα, [N II]/Hα, [O I]/Hα, and [O III]/Hβ. Spaxels whose line ratios are most consistent with ionization by galactic H II regions exhibit a narrow range of dynamically cold line-of-sight velocity distributions (LOSVDs) peaked around 25 km s^{-1} corresponding to a galactic thin disk, while those consistent with ionization by active galactic nuclei (AGNs) and low-ionization emission-line regions (LI(N)ERs) have significantly broader LOSVDs extending to 200 km s^{-1}. Star-forming, AGN, and LI(N)ER regions are additionally well separated from each other in terms of their stellar velocity dispersion, stellar population age, Hα equivalent width, and typical radius within a given galaxy. We use our observations to revise the traditional emission-line diagnostic classifications so that they reliably identify distinct dynamical samples both in two-dimensional representations of the diagnostic line ratio space and in a multidimensional space that accounts for the complex folding of the star-forming model surface. By comparing the MaNGA observations to the SDSS single-fiber galaxy sample, we note that the latter is systematically biased against young, low-metallicity star-forming regions that lie outside of the 3″ fiber footprint.

Unified Astronomy Thesaurus concepts: Galaxy kinematics (602)

Supporting material: animation, data behind figure

1. Introduction

Gas is a key component of galaxies, providing the reservoirs of fuel used to form stars and produce the luminous stellar structures that we observe. This gas is present in a variety of forms and phases, from the cold H_2 molecular gas in which stars form to neutral H I gas reservoirs, to warm ionized gas in H II regions and hot ionized gas in the circumgalactic medium. Over the lifetime of a galaxy gas continually cycles between these phases, collapsing into new stars and being expelled by the end products of stellar evolution to begin the process again (see, e.g., Tumlinson et al. 2017; Péroux & Howk 2020, and references therein).

In the warm ionized gas, emissive cooling is achieved via discrete emission from key atomic transitions. Following recombinations in the ionized hydrogen gas, part of this cooling comes from a cascade of energy-level transitions through key emission lines such as Hα λ6564, Hβ λ4863, and others of the Lyman, Balmer, and Paschen series. While less abundant, metals such as oxygen, nitrogen, and sulfur provide another important avenue for cooling via forbidden line emission triggered by collisional excitations within regions of neutral (e.g., [O I]), singly ionized (e.g., [S II]), or multiply ionized gas (e.g., [O III]) overlapping to various degrees with the ionized hydrogen. The observed strength of a given line is a product of a variety of factors including the spectral shape and intensity of the ionizing radiation, the ionization potential of a given ion (e.g., 10.4 eV for singly ionized S^+, 35.2 eV for doubly ionized O^{++}), and the temperature, density, and metal abundance of the gas. The relative strengths of different lines thus provide sensitive diagnostics of the properties of the ionized gas and the astrophysical sources illuminating them.

Baldwin et al. (1981, hereafter "BPT") popularized the analysis of intensity ratios between optical emission lines that are close together in wavelength, and therefore both free from differential dust extinction and easy to observe simultaneously. Veilleux & Osterbrock (1987) and Ho et al. (1997) further developed this framework, leading to some of the most widely used diagnostic ratios including log([N II] λ6585/Hα) (hereafter "*N2*"), log([S II] λ6718 + 6732/Hα) (hereafter "*S2*"), log([O I] λ6302/Hα) (hereafter "*O1*"), and log([O III] λ5008/Hβ)

(hereafter "*R*3"). Dopita et al. (2000) and Kewley et al. (2001) put such observational diagnostics on a firm theoretical footing, using stellar photoionization models to identify a series of relations (see, e.g., Kewley et al. 2019 and references therein) that divide parameter space into regions consistent with "classical" H II regions resulting from young massive stars and regions fueled by radiative shocks or emission from active galactic nuclei (AGNs).

Each of these emission-line diagnostics has its own strengths and weaknesses (see review by Maiolino & Mannucci 2019 and references therein). For instance, the *N*2 line ratio correlates strongly with gas-phase metallicity in galactic H II regions; within the *N*2–*R*3 star-forming sequence the location of a given galaxy is governed largely by the metallicity (increasing which moves a galaxy along the sequence to smaller *R*3 at larger *N*2) while increasing the ionization parameter (i.e., the dimensionless ratio between the number of hydrogen ionizing photons and the hydrogen density) moves a galaxy across the sequence to larger *R*3 at larger *N*2. However, the *N*2 diagnostic can also be biased by unusual variations in the nitrogen abundance and does less well at distinguishing between other common sources of ionizing photons. In contrast, the *S*2 and *O*1 diagnostics are robust against nitrogen abundance variation and more cleanly distinguish between ionization sources ascribed to AGNs and low-ionization emission-line regions (LI(N)ERs; see, e.g., Dopita 1995). While the former category is relatively well understood to result from energetic feedback derived from a central active nucleus, the LI(N)ER category is more of a historical classification corresponding to galaxies with strong low-ionization emission lines (e.g., [N II], [S II], and [O I]) and (compared to AGNs) relatively weak higher ionization lines such as [O III]. Although such regions were originally observed in the centers of galaxies (e.g., Heckman 1980), recent observations have shown that LI(N)ER-type line ratios occur at larger galactocentric distances as well (Sarzi et al. 2010) and display relatively flat ionization parameter gradients (Yan & Blanton 2012), suggesting that they are generally unrelated to AGN activity. Belfiore et al. (2016) further distinguished between "cLIER" galaxies (i.e., those with LI(N)ER-like emission at small radii and H II regions at larger radii) and "eLIER" galaxies (i.e., those with LI(N)ER-like emission throughout the galaxy and no evidence for significant star formation at any radius).

Complicating these categories is the presence of a substantial amount of Hα emission (30% or more of the integrated emission for a given galaxy) from so-called diffuse ionized gas (DIG), also known as the warm ionized medium (WIM), which in the Milky Way is known as the Reynolds layer (Reynolds 1990). Similar to LI(N)ERs, DIG emission exhibits enhanced *N*2, *S*2, and *O*1 line ratios with respect to galactic H II regions. Although the source of the ionizing photons illuminating the DIG is uncertain, Zhang et al. (2017) argue in favor of post-asymptotic-giant-branch (post-AGB) stars as the dominant mechanism in general because radiation escaping from H II regions is not hard enough to produce the observed line ratios.

Consequently, while strong line ratios are easy to measure, they can be challenging to interpret in terms of the underlying physical origins of the ionizing photons (see, e.g., the review by Sánchez 2020). First and foremost, line ratios can vary dramatically within individual galaxies with gas in different regions ionized by a variety of different mechanisms. Such spatial variations are lost in spectroscopic surveys that do not spatially resolve individual regions within galaxies (e.g., the original SDSS single-fiber survey; Kauffmann et al. 2003; Brinchmann et al. 2004; Tremonti et al. 2004), resulting in line ratios produced by the blending of various components. Additionally, while stellar photoionization models exhibit a characteristic folding of the ionization surface (see discussion in Section 6) the precise upper envelope of the star-forming sequence is confused by contributions from DIG and the overlap with AGN and LI(N)ER models, further complicating efforts to separate different physical mechanisms.

A key additional diagnostic can therefore be provided by spatially resolved integral-field unit (IFU) spectroscopic measurements of the gas-phase velocity dispersion $\sigma_{\mathrm{H}\alpha}$. Star formation generally happens in H II regions with an intrinsic thermal broadening of $\sim$9 km s^{-1} (e.g., Osterbrock 1989) and a potentially comparable nonthermal expansion component; on kiloparsec scales encompassing many such regions, the additional broadening provided by the velocity dispersion between individual H II regions in the galactic thin disk produces an observed $\sigma_{\mathrm{H}\alpha} \sim 15$–30 km s^{-1} (e.g., Jimenez-Vicente et al. 1999; Rozas et al. 2000, 2002; Relano et al. 2005; Andersen et al. 2006). Other ionization mechanisms in contrast trace gas clouds with large-scale streaming motions or extended three-dimensional distributions, and consequently possessing different velocities that produce a broader integrated $\sigma_{\mathrm{H}\alpha}$ of 50 km s^{-1} or more. We therefore expect the line-of-sight velocity distribution (LOSVD) to directly measure the dynamical properties of the ionized gas and thereby help to constrain the physical mechanisms likely to be ionizing that gas.

Multiple studies in the last decade have explored exactly such correlations. Some of the earliest used IFU observations of luminous and ultraluminous infrared galaxies ((U)LIRGs), with Monreal-Ibero et al. (2006, 2010) and García-Marín et al. (2006) noting the positive correlation between $\sigma_{\mathrm{H}\alpha}$ and the *N*2, *S*2, and *O*1 line ratios, which they interpret as evidence for the contribution of shocks. Similarly, Rich et al. (2011) found a bimodal distribution of velocity dispersions in a study of two nearby LIRGs with peaks above and below 50 km s^{-1} that they identified as corresponding to ionized gas in unresolved H II regions and high-velocity shocks, respectively. More recently, Oparin & Moiseev (2018), D'Agostino et al. (2019), and López-Cobá et al. (2020) used the correlation between $\sigma_{\mathrm{H}\alpha}$ and the degree of excitation observed in a handful of nearby galaxies to propose that $\sigma_{\mathrm{H}\alpha}$ be used as an additional diagnostic to help distinguish gas photoionized by H II regions from AGNs and shock-driven excitation mechanisms (see also Zhang & Hao 2018). Targeted studies using the MUSE instrument on the VLT have been able to push this work even further. Della Bruna et al. (2020) for instance noted that the DIG in NGC 7793 had a higher amount of turbulence than the H II regions, while den Brok et al. (2020) used observations of 41 star-forming galaxies to note that the asymmetric drift of the DIG suggested that it was distributed throughout a layer thicker than the star-forming disk but thinner than the stellar disk.

In order to characterize such correlations in detail, however, it is necessary to employ large and representative galaxy samples that cover both the star-forming and quiescent galaxy sequences. Some of the earliest IFU galaxy surveys were unable to explore such correlations in detail as the $R = 850$ spectral resolution of the Calar Alto Legacy Integral Field Area Survey (CALIFA; Sánchez et al. 2012a) at Hα wavelengths was too low to be able to measure velocity dispersions of

typical current-epoch galactic disks, while the $R\sim1200$ Atlas3D survey (Cappellari et al. 2011) focused exclusively on early-type galaxies. With the current generation large-scale IFU galaxy surveys such as MaNGA (Bundy et al. 2015) and SAMI (Croom et al. 2012), however, it is now possible for the first time to study statistically large and representative samples of nearby galaxies with spatially resolved spectroscopy. The MaNGA survey (Bundy et al. 2015) in particular offers an excellent opportunity to study the dynamical properties of ionized gas across a wide range of galaxy populations, as it combines an order-of-magnitude increase in sample size compared to previous IFU surveys with contiguous spectral coverage throughout the $\lambda\lambda$3600–10300 Å wavelength range.

In Section 2 we describe the MaNGA galaxy sample, data reduction process, and the survey data products used in our analysis. In Section 3 we describe the observed relation between the line-of-sight gas-phase velocity dispersion $\sigma_{\rm H\alpha}$ and characteristic strong emission-line flux ratios, defining a new set of empirical functions that separate spaxels into dynamically cold and warm populations. We summarize the physical properties of these populations in Section 4, noting exceptionally strong correspondence between our new dynamically defined selection criteria and a variety of other physical observables (e.g., stellar population age, Hα equivalent width, and radial location) whose relations to strong line flux ratios have been extensively discussed in the literature. We discuss sample-dependent biases in Section 5 and note in particular a significant systematic bias against young, rapidly star-forming regions in low-mass galaxies in the original SDSS-I sample compared to the MaNGA IFU sample in Section 5.4. In Section 6 we discuss our results in the context of theoretical photoionization models and extend our analysis in Section 7 by considering the folding of the photoionization surface in multiple dimensions. We summarize our conclusions in Section 8. Throughout our analysis, we adopt a Chabrier (2003) stellar initial mass function and a ΛCDM cosmology in which $H_0=70\,{\rm km\,s^{-1}\,Mpc^{-1}}$, $\Omega_m=0.27$, and $\Omega_\Lambda=0.73$.

2. Observational Data

The SDSS-IV (Blanton et al. 2017) Mapping Nearby Galaxies at APO (MaNGA) galaxy survey has been described thoroughly in the literature via a series of technical papers. In brief, MaNGA uses custom IFU fiber bundles (Drory et al. 2015) in conjunction with the BOSS spectrographs (Smee et al. 2013) on the Sloan 2.5 m telescope (Gunn et al. 2006) to obtain spatially resolved spectroscopy at spectral resolution $R\sim2000$ throughout the wavelength range $\lambda\lambda$3600–10300 Å. The MaNGA observing strategy and first-year survey data characteristics are described by Law et al. (2015) and Yan et al. (2016), respectively. MaNGA data processing occurs in two stages: a Data Reduction Pipeline (DRP) that produces science-grade calibrated spectroscopic data cubes from the raw observational data (Law et al. 2016, 2021; Yan et al. 2016) and a data analysis pipeline (DAP) that uses PPXF (Cappellari 2017) to produce maps of derived astrophysical quantities from the calibrated data cubes (Belfiore et al. 2019; Westfall et al. 2019). The MARVIN data interface framework provides a responsive Python-based toolkit for interacting with the MaNGA data products both via a web interface and programmatic queries (Cherinka et al. 2019).

As discussed by Wake et al. (2017), the MaNGA galaxy sample is chosen to span both the red sequence and the star-forming main sequence and follow a nearly flat stellar mass distribution in the range $M_*=10^9$–$10^{11}M_\odot$. These galaxies are broken into a primary sample covering galaxies out to 1.5 effective radii ($1.5R_{\rm e}$), a secondary sample covering out to $2.5R_{\rm e}$, and a color-enhanced sample designed to more extensively populate lower-density regions of color–magnitude space (e.g., the "green valley"). These samples are selected without regard to galaxy morphology or the presence of AGNs, although a variety of smaller ancillary samples within the MaNGA survey (∼15% of the total number of data cubes) explicitly target unique galaxy classes such as major mergers, edge-on disks, AGNs, dwarf galaxies, etc.

For the present analysis, we use data products from the final MaNGA internal data release version MPL-11. These data products are identical to those that will be released publicly in SDSS Data Release DR17 and similar to those in MPL-10 discussed by Law et al. (2021) except for a larger total sample size (see a summary of all previous versions provided by Law et al. 2021, their Table 1). Starting with the 11,273 galaxy data cubes in MPL-11, we downselect to the 10,296 cubes that are not part of ancillary programs targeting small regions within the M31 or IC 342 galaxies, or that target intracluster light, ultrafaint dwarfs, or other unusual objects in the Coma cluster (see, e.g., Gu et al. 2018). We additionally discard 158 data cubes flagged by the DRP/DAP as having significant reduction problems, 119 data cubes for which the galaxy was deliberately miscentered in the IFU by more than 1″ (as part of various ancillary programs), and 3 data cubes for galaxies at redshift z below 0.001 to ensure a more consistent range of redshifts for the sample. This leaves a sample of 10,016 data cubes, of which 9883 are unique galaxies and a small number have one to two repeat observations for cross-calibration purposes. As illustrated in Figure 1 these galaxies span three orders of magnitude in stellar mass and four orders of magnitude in total star formation rate.[14]

At $R\sim2000$ the MaNGA hardware delivers a 1σ instrumental velocity resolution of about $70\,{\rm km\,s^{-1}}$, posing a substantial challenge for the accurate recovery of astrophysical velocity dispersions of ∼15–30 $\rm km\,s^{-1}$ for galactic thin disks, especially because the instrumental resolution is known to vary with both time and the gravitational flexure of the spectrographs. As discussed at length by Law et al. (2021), however, the improvements in calibration in MPL-10 enable exquisite characterization of the instrumental response, allowing us to push scientific analyses down to velocity dispersions that are typically prohibitively difficult to measure for comparable resolution instruments. Based on comparisons against high-resolution ($R\sim10{,}000$) external observations, Law et al. (2021) find that the MPL-10 time-dependent spectral line spread function (LSF) provided by the DRP is accurate to 0.6% (systematic) with 2% random uncertainty and that the resulting Hα velocity dispersions provided by the MaNGA DAP have an uncertainty of about $1\,{\rm km\,s^{-1}}$ (systematic) and $5\,{\rm km\,s^{-1}}$ (random) at $\sigma_{\rm H\alpha}=20\,{\rm km\,s^{-1}}$ for lines detected at a signal-to-noise ratio $({\rm S/N})>50$. Repeating the analyses of Law et al. (2021), we find results that are statistically unchanged for MPL-11.

[14] Effective radii and stellar masses are drawn from the parent galaxy catalog described by Wake et al. (2017) based on an extension of the NASA-Sloan Atlas (NSA; Blanton et al. 2011). Star formation rates are estimated from the integrated Hα flux in the MaNGA data.

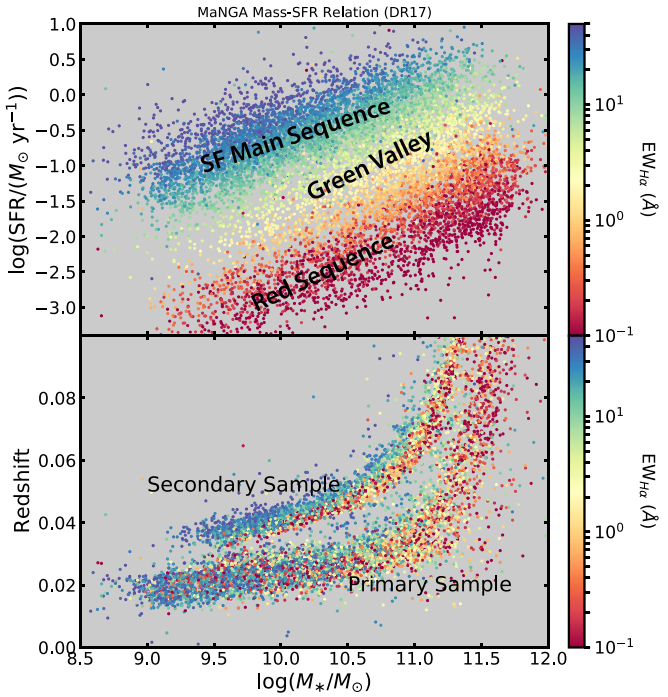

Figure 1. Stellar mass vs. redshift and total Hα-derived SFR (uncorrected for dust extinction) within the IFU field of view for the MaNGA MPL-11 galaxy sample. Each point represents one of the ∼10,000 galaxies in MPL-11, and are color-coded by their integrated Hα equivalent width. The Primary ($1.5R_e$) and Secondary ($2.5R_e$) samples define a clearly offset trend in redshift at fixed stellar mass.

In our present analysis we use the Hα velocity dispersion maps produced by the MaNGA DAP (Belfiore et al. 2019; Westfall et al. 2019) using the "hybrid" binning scheme in which stellar continuum measurements are made on galaxy data cubes that have been Voronoi-binned (Cappellari & Copin 2003) to a minimum g-band continuum S/N of 10 Å^{-1}, while emission-line measurements are made for each individual 0.″5 spaxel in the data cubes. The stellar continuum templates used for fitting the emission lines (see further discussion in Section 5.3) are based on a series of hierarchically clustered template spectra observed by the MaNGA MaStar program (Yan et al. 2019). We reject individual spaxel measurements with bad data quality flags set for either the Hα flux, velocity, or velocity dispersion, and likewise reject ∼100 spaxels in the MPL-11 sample with the DAP-reported Hα flux in the range 10^{-13}–10^{-5} erg s^{-1} cm^{-2} spaxel $^{-1}$ as these represent unmasked noise artifacts.

Additionally, we correct the velocity dispersion maps provided by the DAP for beam smearing following the method described by Law et al. (2021). In brief, this method involves estimating the magnitude of beam smearing by convolving a model velocity field with the known point-spread function and subtracting the artificial component of the velocity dispersion in quadrature from the observed values. The magnitude of this correction varies depending on the velocity field of a given galaxy, but for $\sigma_{\rm H\alpha} < 40$ km s^{-1}, the median correction due to beam smearing is 9%, with 90% of spaxels having a correction of less than 25%.

3. Defining Dynamical Samples

Using the maps of strong emission-line fluxes produced by the DAP, we plot in Figure 2 (middle panels) the density distribution of MaNGA spaxels for a 100×100 pixel grid in the classical line ratio diagnostics $N2 = \log([\text{N II}]\ \lambda6583/\text{H}\alpha)$, $S2 = \log([\text{S II}]\ \lambda6716 + 6731/\text{H}\alpha)$, and $O1 = \log([\text{O I}]\ \lambda6300/\text{H}\alpha)$ versus $R3 = \log([\text{O III}]\ \lambda5007/\text{H}\beta)$.[15] In each panel we have selected all spaxels from the galaxy sample for which the relevant emission lines have all been detected with S/N > 5 and whose Hα velocity dispersions are greater than zero after correcting for both beam smearing and the instrumental LSF.[16] For the [N II]/Hα and [S II]/Hα diagrams, this results in a sample size of about 3.6 million spaxels[17] distributed across 7400 galaxies, while the [O I]/Hα diagram contains about a factor of 3 fewer total spaxels (1.2 million spaxels across 6300 galaxies) because [O I] is generally fainter than either [N II] or [S II]. These samples are subject to significant selection effects, the biases of which we address in detail in Section 5.

As discussed at length by Belfiore et al. (2016), the spatially resolved SDSS/MaNGA data in Figure 2 show similar trends to those observed in earlier-generation SDSS single-fiber spectroscopy (e.g., Kauffmann et al. 2003; Brinchmann et al. 2004; Tremonti et al. 2004). The well-defined sequence at the lower left corresponds to ionizing photons emitted by young massive stars in galactic H II regions, while the extended regions toward the top right of the diagram correspond to gas illuminated by photons with a harder spectrum emitted by a combination of AGNs, dynamical shocks, and LI(N)ER-like sources. The traditional star-forming sequence in the [N II]/Hα diagram is bounded by the empirical number density relation given by Kauffmann et al. (2003; black dotted line in Figure 2). Another commonly used set of relations is that given by Kewley et al. (2001; black dashed lines in Figure 2), who used photoionization models to compute a series of theoretical "maximum starburst" relations in each of the [N II]/Hα, [S II]/Hα, and [O I]/Hα projections.

For each bin in the [N II]/Hα, [S II]/Hα, and [O I]/Hα diagrams containing more than 5 spaxels, we compute the sigma-clipped mean Hα velocity dispersion $\sigma_{\rm H\alpha}$, and plot the resulting trends in Figure 2 (lower panels).[18] We immediately note that the traditional star-forming sequence (as defined by either the [N II]/Hα relation of Kauffmann et al. 2003 or the [S II]/Hα relation of Kewley et al. 2001) is extremely well defined, with median gas-phase velocity dispersion $\sigma_{\rm H\alpha} < 40$ km s^{-1} throughout a wide range of line ratios. At higher $N2$, $S2$, or $O1$ line ratios the velocity dispersion rises rapidly, reaching values of 100–200 km s^{-1} in regions typically associated with AGN or LI(N)ER emission. Given this strong correlation between the sources of the ionizing photons and the LOSVD of the gas illuminated by these photons, we therefore explore whether it is possible to use our kinematic data (which is broadly representative of the low-redshift galaxy population) to define

[15] Throughout this manuscript we follow the use in which [N II] refers specifically to the [N II] λ6583 intensity, while [S II] refers to the sum of the [S II] λ6716 and λ6731 intensities. Likewise, $N2$, $S2$, $O1$, and $R3$ refer to the logarithmic line intensity ratios, while [N II]/Hα, [S II]/Hα, and [O I]/Hα refer to the relevant diagnostic diagrams.

[16] Rejection of spaxels with zero or imaginary velocity dispersions after quadrature subtraction of the instrumental LSF and beam smearing rejects just 5% and 2% of the total sample, respectively.

[17] Because individual spaxels are 0.″5 in size and the MaNGA PSF has an FWHM of about 2.″5, there is thus significant correlation between adjacent spaxels in a given galaxy. Conservatively, this corresponds to ∼300,000 statistically independent spaxels, although in practice the number is higher because not all spaxels in a given resolution element meet our S/N threshold.

[18] FITS representations of the density and mean Hα velocity dispersion plots can be found in the supplementary data.

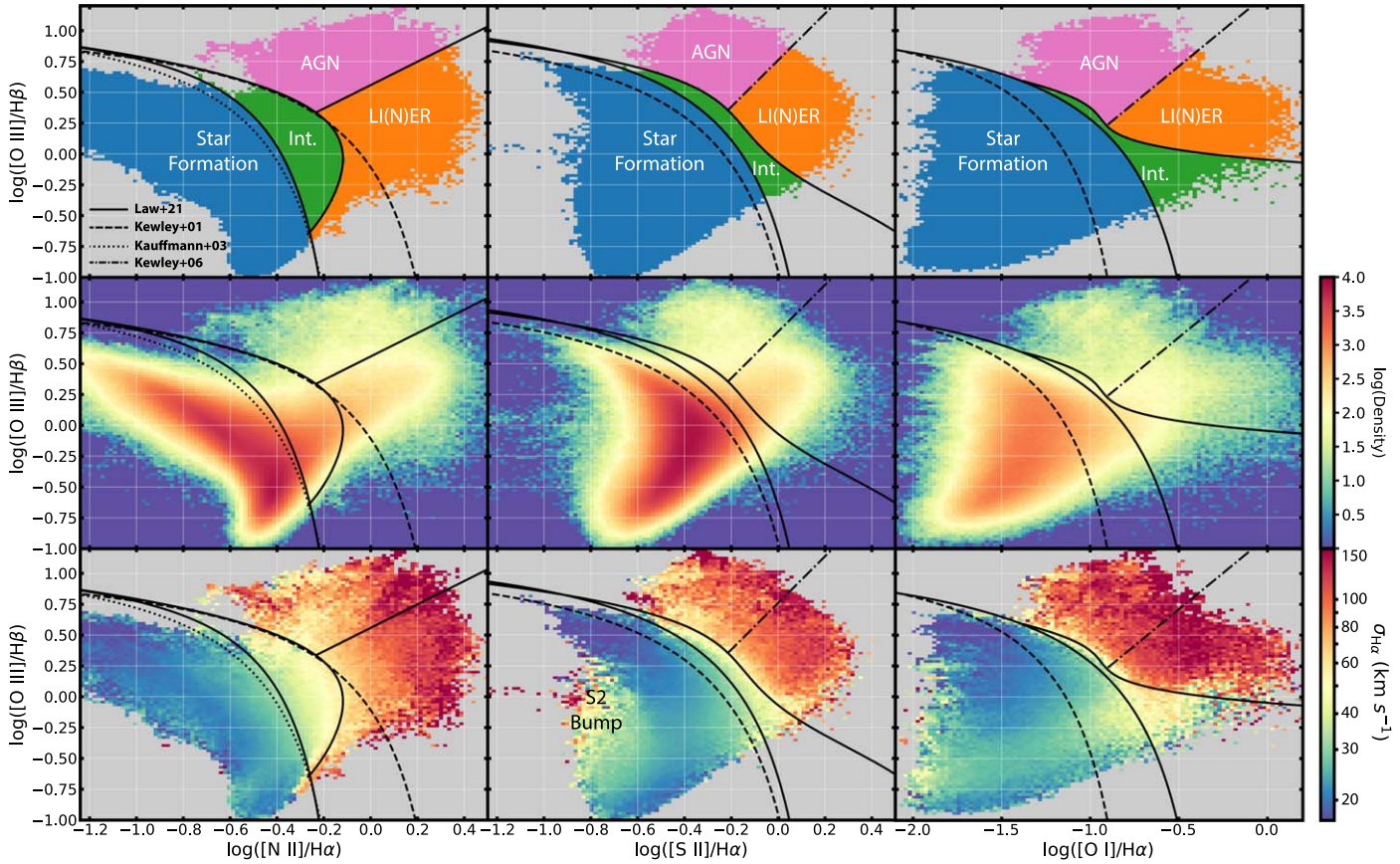

Figure 2. Top panels: classification of the [N II]/Hα, [S II]/Hα, and [O I]/Hα diagnostic diagrams into four regions (star-forming, intermediate, AGN, and LI(N)ER) based on their observed dynamical properties. Middle panels: number density of spaxels with a given diagnostic nebular emission-line ratio for all spaxels in MPL-11 whose emission lines are detected with S/N > 5 (∼3.6 million spaxels from 7400 individual galaxies). The star-forming sequence is clearly defined as the red peaks in the density distribution, while lower-density regions trace emission-line ratios typically associated with active galactic nuclei or LI(N)ER emission. Bottom panels: as above, but color-coded by the sigma-clipped mean Hα velocity dispersion of the MaNGA spaxels at a given line ratio. In all panels the black solid curves represent empirical polynomial fits tracing the $\sigma_{H\alpha} = 35$ and 57 km s^{-1} ionized gas isodispersion contours (see discussion in Section 3), while the black dashed lines represent the theoretical maximum-starburst relations defined by Kewley et al. (2001). Black dotted–dashed lines in the [S II]/Hα and [O I]/Hα panels (middle and right columns, respectively) show the empirical density-based Seyfert/LI(N)ER classifications defined by Kewley et al. (2006), while the corresponding black solid line in the [N II]/Hα panel (left columns) is defined in Equation (9). The black dotted line in the [N II]/Hα panels represents the empirical boundary to the star-forming sequence from SDSS single-fiber observations defined by Kauffmann et al. (2003). The data behind this figure are available in a multiextension FITS file in a .tar.gz package.

(The data used to create this figure are available.)

physically distinct subsamples that can help constrain theoretical starburst models.

Starting from the [N II]/Hα relation shown in Figure 2 (left-hand panels), we note that the Kauffmann et al. (2003) relation does a good job of visually tracing the isodispersion contours separating low-$\sigma_{H\alpha}$ regions (blue/green points) from higher-$\sigma_{H\alpha}$ regions (yellow/red points). The average quantities shown here though belie the even more significant differences between the underlying distributions of gas dispersions. We therefore compute the effective distance d_{N2} of a given spaxel in $N2$ versus $R3$ space from the Kauffmann et al. (2003) relation, with negative values defined to represent line ratios below the relation and positive values above the relation.[19] As we illustrate in Figure 3 (top panel), the overall trend in the median $\sigma_{H\alpha}$ from the star-forming to non-star-forming regions is driven not by a gradual shift in the underlying gas kinematics but rather by an abrupt change in the relative weights of two kinematically distinct LOSVDs. At $d_{N2} \leqslant -0.1$ dex, spaxels exhibit a remarkably constant range of velocity dispersions that change only minimally with increasing distance from the Kauffmann et al. (2003) relation. This dynamically cold LOSVD is strongly peaked around $\sigma_{H\alpha} = 24$ km s^{-1} and has a narrow distribution with a half-width of about 11 km s^{-1}. In contrast, at values of $d_{N2} > 0$ dex, $\sigma_{H\alpha}$ is increasingly dominated by an entirely different and much broader LOSVD ranging from $\sigma_{H\alpha} > 30$–150 km s^{-1}. These results are reminiscent of the nearly bimodal distributions observed by Rich et al. (2011) and similarly motivate us to separate the sample into two distinct dynamical populations.

As discussed further in Section 5, any effort to define a single "transition" threshold between dynamically cold and warm LOSVDs is necessarily subjective and dependent on the details of both the sample selection and numerical analysis. We have chosen to use a 2.5σ clipping algorithm for instance to identify the peak of the cold LOSVD, as this method appeared to best reproduce the visual peak shown in Figure 3 in the presence of extended asymmetric tails to the distribution. If we

[19] Using the shortest distance from the curve rather than the distance along the vertical axis; see, e.g., the discussion in Section 4 of Kewley et al. (2006).

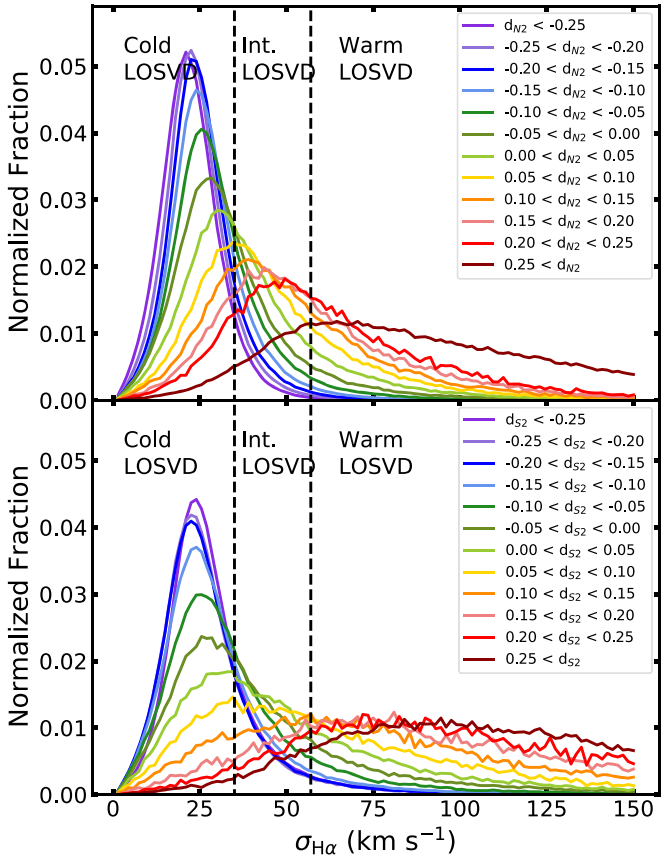

Figure 3. Top panel: histogram of individual spaxel velocity dispersions binned according to their effective distance d_{N2} (measured in dex) from the Kauffmann et al. (2003) classification line in the space of emission-line intensity ratios [N II]/Hα vs. [O III]/Hβ. Bottom panel: as above, but for spaxels binned according to their distance d_{S2} from our kinematically defined classification line in [S II]/Hα vs. [O III]/Hβ space. In both panels the vertical dashed lines denote the 1σ and 3σ wings of the cold gas LOSVD; we use these divisions at $\sigma_{H\alpha} = 35$ and 57 km s^{-1} to split spaxels into dynamically cold, intermediate, and dynamically warm populations.

had instead chosen to use a simple median, a Gaussian-fitting technique or a different kind of sigma clipping our derived centroid would vary only very slightly in the range $\sigma_{H\alpha} = 23$–26 km s^{-1}. We opt not to use a flux-weighted mean as this would effectively bias our sample toward small radii instead of allowing us to compare properties throughout the IFU field of view (see discussion in Section 5.4). In contrast, we used a 5σ clipping algorithm to measure the cold LOSVD profile width in order to better capture the extended tail of the distribution. Using a more or less aggressive approach can change the measured half-width in the range 9–16 km s^{-1}. This width will be driven in part by the significant uncertainty in MaNGA velocity dispersions far below the instrumental limit. Monte Carlo tests suggest that these uncertainties may contribute about 6 km s^{-1} in quadrature (consistent with Figure 15 of Law et al. 2021 for our range of S/N), leaving the astrophysical width in the range 7–15 km s^{-1}.

Given the limitations of the MaNGA data this far below the instrumental resolution, for our present purposes, we simply define the 1σ and 3σ extremes of the well-defined cold LOSVD at $\sigma_{H\alpha} = 35$ and 57 km s^{-1}, respectively, as the approximate transition points to an "intermediate" and a dynamically "warm" gas distribution. Using these thresholds, we define an entirely dynamically based series of classifications for the [N II]/Hα, [S II]/Hα, and [O I]/Hα diagnostic diagrams. For the 1σ lines defining our nominal boundary of the dynamically cold sequence in Figure 2, we fit the isodispersion contours using rectangular hyperbolae of the form defined by Kewley et al. (2001) and find

$$R3 = \frac{0.438}{N2 + 0.023} + 1.222, \quad (1)$$

$$R3 = \frac{0.648}{S2 - 0.324} + 1.349, \quad (2)$$

$$R3 = \frac{0.884}{O1 + 0.124} + 1.291, \quad (3)$$

while for the 3σ lines defining the boundary of the warm sequence we use a fourth-order polynomial as a function of $R3$ in order to satisfactorily fit the wide range in observed behaviors and find

$$N2 = -0.390\,R3^4 - 0.582\,R3^3 - 0.637R3^2 - 0.048\,R3 - 0.119 \quad (4)$$

for $-0.65 < R3 < 1.00$,

$$S2 = -1.107\,R3^4 - 0.489\,R3^3 + 0.580R3^2 - 0.579\,R3 - 0.043 \quad (5)$$

for $-1.10 < R3 < 1.10$, and

$$O1 = 19.021\,R3^4 - 36.452\,R3^3 + 21.741R3^2 - 5.821\,R3 - 0.328 \quad (6)$$

for $-0.25 < R3 < 0.60$.

The resulting fits are shown in Figure 2 as black solid lines. Repeating our earlier analysis of the $N2$ LOSVD histograms as a function of distance from the Kauffmann et al. (2003) relation using instead the offset distance from our newly derived 35 km s^{-1} isodispersion [S II]/Hα relation (Figure 3, lower panel) we find an identical 1σ threshold of $\sigma_{H\alpha} = 35$ km s^{-1} for the cold LOSVD, confirming that our analysis has converged.

For the [N II]/Hα diagram (Figure 2, left-hand column) we note that our 1σ dynamical relation (Equation (1)) is extremely similar to the density-based Kauffmann et al. (2003) relation, albeit protruding to values of $N2$ that are larger by about 0.05 dex. Our 3σ relation (Equation (4)) extends to larger values of $N2$ and initially follows the Kewley et al. (2001) maximum-starburst relation at large $R3$ before looping back to lower values of $N2$ at low $R3$ to accommodate a tail of high $\sigma_{H\alpha}$ spaxels. In contrast, the maximal-starburst line overshoots the dynamically cold population and extends well into the range of $\sigma_{H\alpha} = 50$–100 km s^{-1} that are more consistent with large-scale gas flows or other components that are much thicker than traditional star-forming disks. This finding is in agreement with recent photoionization models such as those by Byler et al. (2017) and F. Belfiore et al. (2021, in preparation), which more closely match both our results and the Kauffmann et al. (2003) line, as shown in Section 6.

For the [S II]/Hα diagram (Figures 2 and 4, middle column) our 1σ relation (Equation (2)) is similar to the Kewley et al. (2001) maximal-starburst line, albeit shifted to larger $S2$ by about 0.15 dex. Our 3σ relation (Equation (5)) in contrast extends nearly linearly toward the bottom right of the diagram, encompassing a narrower range of "intermediate" population spaxels than in the [N II]/Hα diagram.

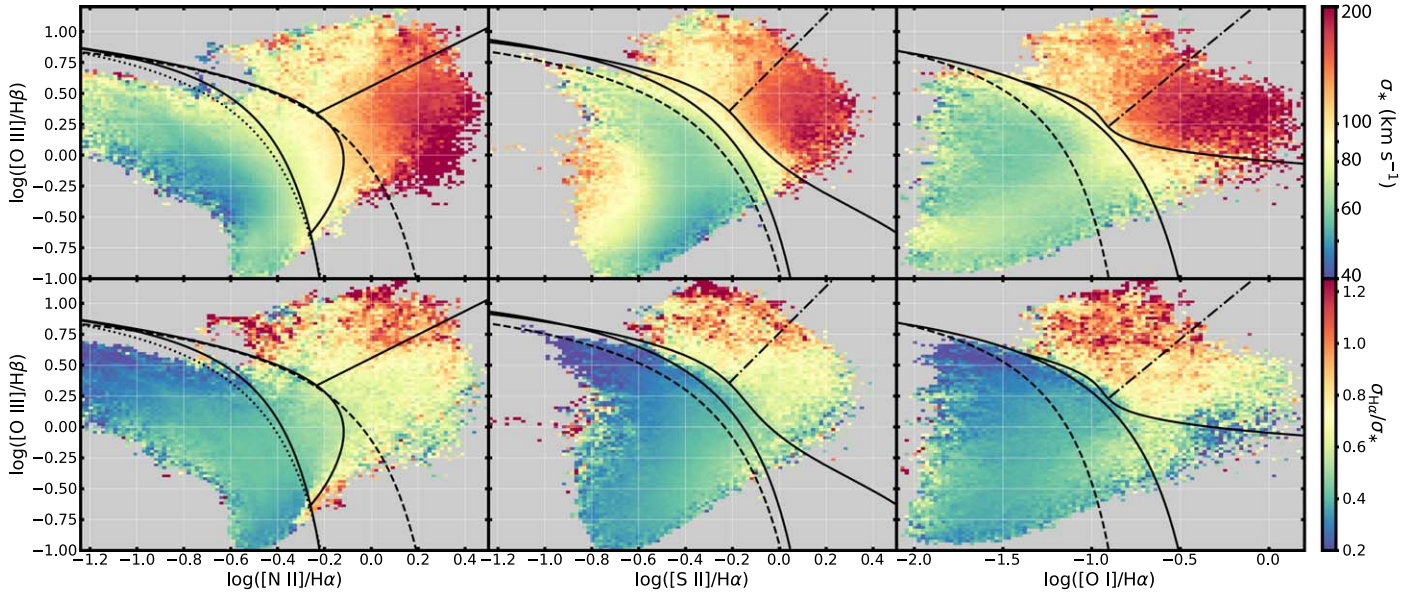

Figure 4. As Figure 2, but showing pixels color-coded by the median stellar velocity dispersion, and the median ratio between gas-phase and stellar velocity dispersion. Note the strong evolution of the relative velocity dispersions in which the ionized gas dispersions are significantly smaller than the stellar dispersion in the star-forming region, only slightly smaller than the stellar dispersions in the LI(N)ER region, and comparable to or in excess of the stellar dispersions in the AGN region.

For the [O I]/Hα diagram (Figures 2 and 4, right-hand column) our 1σ dynamical relation (Equation (3)) extends much higher (nearly 0.3 dex) in $O1$ than the Kewley et al. (2001) relation, although the exact track is somewhat uncertain due to the cluster of higher=$\sigma_{\rm H\alpha}$ values toward low values of $R3$. Our 3σ relation (Equation (6)) differs dramatically from the shape of the [N II]/Hα or [S II]/Hα cases, extending nearly horizontally along the line $R3 = 0.0$ to encompass a wide "intermediate" region at low values of $R3$.

All of these relations are subject to our somewhat arbitrary choice of how to define the boundaries between the dynamically cold, intermediate, and warm kinematic populations. However, our overall conclusions are largely insensitive to such details. If we instead repeat our analysis using a slightly different peak velocity dispersion for the cold LOSVD profile or using a different profile width, the 1σ sequences defined by Equations (1)–(3) change by 0.05 dex or less. Our 3σ sequences defined by Equations (4)–(6) change by as much as 0.08 dex in the $N2$–$R3$ diagram, and less in the $S2$–$R3$ diagram.

From a dynamical point of view, the cleanest sample of spaxels with gas-phase velocity dispersions akin to those of H II regions in a cold disk can thus be obtained using our empirical 1σ relations in either [N II]/Hα, [S II]/Hα, or [O I]/Hα line ratio space. In a practical sense, our [N II]/Hα selection method is nearly equivalent to the classical Kauffmann et al. (2003) method, our [S II]/Hα selection method is broadly similar to the Kewley et al. (2001) method but includes a slightly larger range in [S II]/Hα, and our [O I]/Hα selection method differs dramatically from any previous relations.

4. Physical Properties of the Dynamical Samples

Having defined three dynamically distinct samples (i.e., cold, intermediate, and warm) in Section 3, we next consider how these populations compare in terms of other physical properties. In doing so, we additionally include one more physical division in the warm population between the AGN-like and the LI(N)ER-like spaxels. For the [S II]/Hα and [O I]/Hα diagrams we simply adopt the empirical density-based relations given by Kewley et al. (2006) in which

$$R3 = 1.89 \times S2 + 0.76 \quad (7)$$

for values of $-0.22 < S2 < 0.3$ (i.e., meeting our 3σ boundary of the "intermediate" region), and

$$R3 = 1.18 \times O1 + 1.30 \quad (8)$$

for values of $-0.9 < O1 < 0.3$. Additionally, we define a new and similar relation for the [N II]/Hα diagram:

$$R3 = 0.95 \times N2 + 0.56 \quad (9)$$

for $-0.24 < N2 < 0.5$ (see discussion in Section 4.2).

We explore the physical interpretation of the trends observed in Figure 2 by using the DAP maps in a similar manner to calculate the mean stellar velocity dispersion, the ratio of the stellar and gas-phase velocity dispersion, the Hα equivalent width, the median strength of the 4000 Å break (D_n4000, i.e., a proxy for stellar population age; Balogh et al. 1999), the spaxel radius as a fraction of the galaxy effective radius ($R/R_{\rm eff}$), and the host galaxy stellar mass. We illustrate the two-dimensional distribution of each of these characteristics in the [N II]/Hα, [S II]/Hα, and [O I]/Hα diagrams in Figures 4 and 5, and plot the overall distributions within each of our four regions in Figure 6. We note that many of the trends illustrated by Figure 5 in particular are well established in the literature (see, e.g., Sánchez 2020, and references therein) and provide important context for our new dynamical results.

4.1. Properties of the Dynamically Cold Sample

We consider first those galaxy spaxels within the dynamically cold population below our 35 km s^{-1} isodispersion line; these correspond to emission-line ratios within the classical star formation region. As discussed in the previous section, not only is the mean gas-phase velocity dispersion in this region less than in other regions (see, e.g., Figure 2), but the overall distribution of values is substantially narrower as well (Figure 6). The majority of

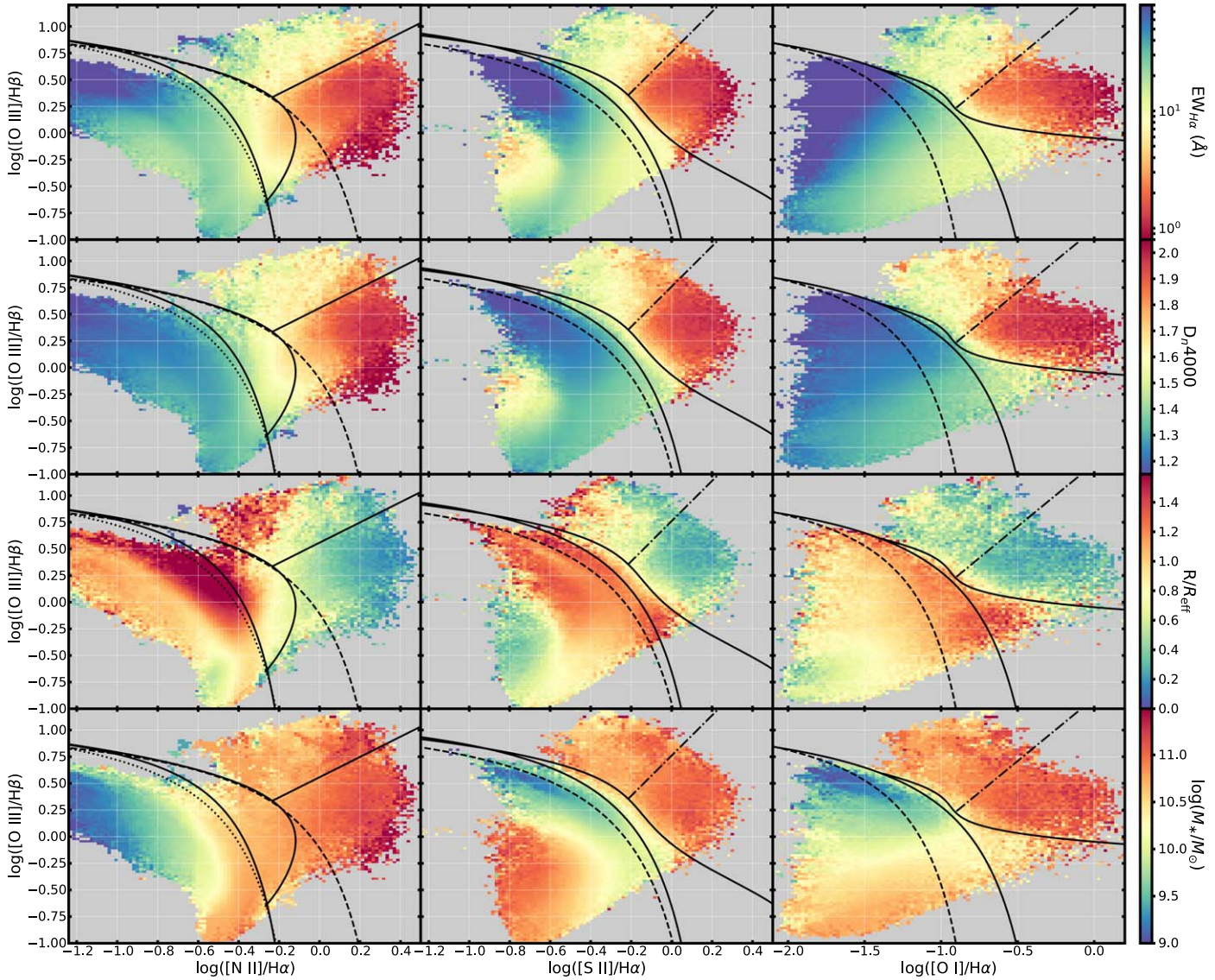

Figure 5. As Figure 2, but showing pixels color-coded by the median Hα equivalent width, D_n4000 spectral break strength, radius (given as a fraction of the host galaxy effective radius R_e), and host galaxy stellar mass for all MaNGA MPL-10 galaxy spaxels meeting our selection criteria. Although our classification lines (solid black lines) were defined using solely dynamical criteria, they nonetheless trace clear boundaries in a variety of other physical observables as well.

all star-forming spaxels have LOSVDs $\sigma_{H\alpha}$ in the range $15-35\,\mathrm{km\,s^{-1}}$ consistent with a population of H II regions embedded within a dynamically cold gas disk. These gas-phase dispersions are typically about 40% of the corresponding stellar velocity dispersion, which peaks at values of $\sigma_* \sim 50$–$60\ \mathrm{km\,s^{-1}}$ corresponding to a composite thin+thick stellar disk.

Based on Figures 5 and 6, these spaxels unsurprisingly (see, e.g., Belfiore et al. 2016; Sánchez 2020, their Figures 3 and 1, respectively) have large Hα equivalent widths, $\mathrm{EW}_{H\alpha} > 10$Å, and lie almost exclusively within galaxies whose globally integrated equivalent widths are typical of the late-type star-forming galaxy population in Figure 1. Likewise, these spaxels tend to have a weak 4000 Å break consistent with a stellar population age of less than $\sim$1 Gyr for reasonable stellar population models (see, e.g., Noll et al. 2009), and to lie at predominantly large radii $\sim 1R_e$ consistent with inside-out models of galaxy growth. Such star-forming spaxels are hosted by galaxies across a wide range of stellar masses, $M_* = 10^9$–$10^{11} M_\odot$, for which the nearly flat mass distribution is a consequence of the MaNGA sample selection (see Wake et al. 2017 for details).

As illustrated in Figure 5 (bottom-left panel) the host galaxy mass clearly correlates well with the observed $N2$ line ratio (i.e., because $N2$ is a proxy for metallicity, the MaNGA spaxels follow a well-defined mass–metallicity relation; see, e.g., Tremonti et al. 2004). A similar trend is apparent in the [N II]/Hα projection of $\sigma_{H\alpha}$ as well, implying a positive correlation such that $\sigma_{H\alpha}$ increases monotonically from 20 to $30\,\mathrm{km\,s^{-1}}$ with increasing stellar mass. Such correlations between $\sigma_{H\alpha}$ and stellar mass (or alternatively, with star formation rate) have been noted previously by other groups (e.g., Green et al. 2014; Krumholz et al. 2018; Varidel et al. 2020); we defer a detailed discussion of such trends within the star formation sequence to a forthcoming publication.

Figures 2, 4, and 5 also demonstrate that the three [N II]/Hα, [S II]/Hα, and [O I]/Hα diagnostic diagrams are not equivalent in terms of their ability to pick out a pure sample of star-forming spaxels. For instance, the [S II]/Hα diagram shows clear evidence of a region that we term the "$S2$ bump" within the nominally star-forming region around $S2 = -0.8$ and $R3 = 0$. Spaxels with emission-line ratios placing them in this region have abnormally weak Hα equivalent widths, strong 4000 Å breaks, lie at smaller

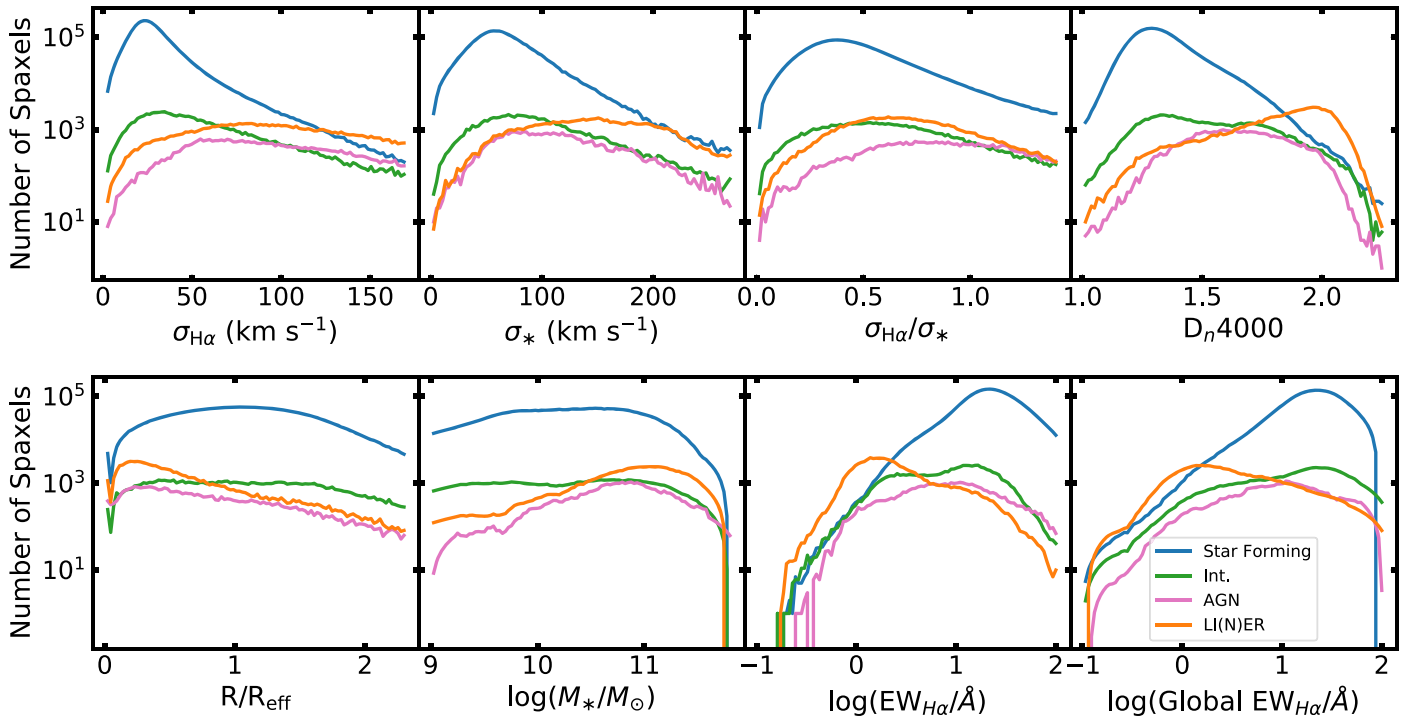

Figure 6. Histograms of galaxy properties in each of the four classes (star-forming, intermediate, AGN, and LI(N)ER) in the [S II]/Hα diagnostic diagram defined by Figure 2. Individual panels show distributions both in the properties of individual spaxels and in the overall galaxy-integrated stellar mass and global equivalent width of the host galaxies within which individual spaxels reside. Histograms for total galaxy mass and equivalent width have been lightly smoothed by a Savitzky–Golay filter to minimize high-frequency artifacts from the discrete integrated values across multiple spaxels.

radii ($< 0.5R_e$) in higher-mass galaxies ($M_* > 10^{10.5}M_\odot$), and have higher stellar ($\sigma_* = 80$–90 km s^{-1}) and gas-phase ($\sigma_{H\alpha} = 50$ km s^{-1}) velocity dispersions than any spaxels in the *N*2-defined star-forming region. A similar feature is visible in the [O I]/Hα diagram as well but manifests more as a gradient in each of the above quantities in *R*3 at fixed *O*1.

As we demonstrate in Section 7, such features are a consequence of the complex folding of the multidimensional photoionization hyper-surface, which can produce unusual artifacts when projected into two dimensions (see, e.g., Figure 11 of Kewley et al. 2019). The ultimate impact of this unusual group of spaxels is likely minimal for most observational studies (because the relative number density of spaxels in the bump is two to three orders of magnitude lower than in the peak of the star-forming sequence) but is nonetheless of interest in constraining numerical models. We return to this discussion in Sections 6 and 7.

4.2. Properties of the LI(N)ER Sequence

At the largest *S*2, *N*2, or *O*1 line ratios, stellar populations models (e.g., Kewley et al. 2001) suggest that the ionizing radiation from young stars is inadequate to produce the observed strength of the [N II], [S II], and [O I] low-ionization emission lines. The origin of the photons ionizing the gas in such LI(N)ER regions has thus been debated in the literature as some combination of faint AGN (e.g., Heckman 1980; Kewley et al. 2006), reprocessed leakage from H II regions (e.g., Mathis 1986; Domgorgen & Mathis 1994; Flores-Fajardo et al. 2011), radiative shocks (Dopita 1995), or a radially extended population of other ionizing sources (e.g., Binette et al. 1994; Yan & Blanton 2012). Most recently, numerous authors have favored this latter interpretation given the observed radial surface brightness profiles of the Balmer emission lines (Sarzi et al. 2010; Yan & Blanton 2012), with photoionization from hot evolved post-AGB stars emerging as a leading candidate (see, e.g., Binette et al. 1994; Sarzi et al. 2010; Singh et al. 2013; Belfiore et al. 2016; Zhang et al. 2017; Byler et al. 2019).

As illustrated by Figure 2, our 3σ isodispersion criterion defined in Equations (4)–(6) identifies a set of spaxels with large gas-phase velocity dispersions and a range of line ratios consistent with the LI(N)ER galaxy population. Figures 4 and 5 show that this dynamically defined boundary also excellently reproduces visible boundaries between the LI(N)ER and other regions in terms of physical observables such as D_n4000, effective radius, stellar velocity dispersion, and host galaxy mass (particularly for the [S II]/Hα and [O I]/Hα projections). This general agreement across a variety of independent quantities reinforces our interpretation of this boundary as one of physical significance. Similarly, these quantities likewise show significant differences across the [S II]/Hα and [O I]/Hα AGN/LI(N)ER dividing lines (Equations (7) and (8)) proposed by Kewley et al. (2006) as well. Although the AGN and LI(N)ER regions are not as well separated in the [N II]/Hα diagram as in the [S II]/Hα or [O I]/Hα diagrams, because they still show broadly similar distinctions we therefore define a comparable [N II]/Hα relation in Equation (9) that can be used if observations of the [S II] or [O I] lines are not available.

Figure 6 demonstrates that those spaxels in our dynamically defined LI(N)ER region have predominantly low Hα equivalent widths and strong 4000 Å breaks indicative of a $\sim$10 Gyr old stellar population. Similarly, while they occur primarily in high-mass galaxies whose galaxy-integrated Hα equivalent widths place them on the red sequence (see Figures 6 and 1), there is a tail to the distribution down to lower masses and global equivalent widths $\sim$10 Å that overlaps with the ordinary star-forming galaxy population. Given that galaxies with small

total Hα luminosities have low S/N it is probable that the apparent lower boundary to the LI(N)ER equivalent widths in Figure 6 is simply an artifact of our S/N > 5 spaxel selection criterion, and that observations deeper than the MaNGA survey spectra would extend the LI(N)ER sample well into the early-type red-sequence population (see Section 5.3 and Figure A1 of Belfiore et al. 2016).

These results are generally consistent with previous observations by (e.g.,) Cid Fernandes et al. (2010), Yan & Blanton (2012), Belfiore et al. (2016), and Sánchez et al. (2021). With the aid of the MaNGA kinematics we can determine (e.g., Figure 6) that both the stellar and gas-phase velocity dispersions of our LI(N)ER sample span a wide range $\sigma_* = 100$–200 km s^{-1} and $\sigma_{\rm H\alpha} = 50$–$150$ km s^{-1}, respectively, with the median peaked around $\sigma_{\rm H\alpha}/\sigma_* = 0.6$. These velocity dispersions are inconsistent with gas distributed in a thin disk and more consistent with bulges or other largely pressure-supported systems, suggesting that our dynamical LI(N)ER sample predominantly traces a diffuse WIM with a large vertical scale height broadly resembling that of the stars. This conclusion is further supported by the clear correlations between $\sigma_{\rm H\alpha}$, spaxel radius, and host galaxy mass in the sense that the highest values of $\sigma_{\rm H\alpha} > 150$ km s^{-1} occur almost exclusively at $R < R_{\rm eff}$ and $M > 10^{10.5} M_\odot$.

4.3. Properties of the Intermediate Sequence

The Intermediate region is defined as lying between the 1σ and 3σ wings of the star-forming population, with mean gas-phase velocity dispersion between $\sigma_{\rm H\alpha} = 35$ km s^{-1} and 57 km s^{-1}. Figure 2 illustrates that the shape and size of this region vary considerably; in the [N II]/Hα diagram it measures roughly 0.2 dex in width, tapering slightly toward the top of the AGN and the bottom of the LI(N)ER distributions. In the [S II]/Hα diagram the Intermediate region is significantly narrower in general, but flares to be wider between the star formation and LI(N)ER sequences than between the star formation and AGN sequences. In contrast, in the [O I]/Hα diagram the Intermediate region is extremely narrow between the star-forming and AGN sequences, but the dividing line becomes nearly horizontal around $R3 = 0.0$, encompassing a range of values roughly 1 dex wide between the star-forming and LI(N)ER sequences.

In terms of the gas-phase velocity dispersions, individual spaxels in the Intermediate region range from $\sigma_{\rm H\alpha} = 20$–$100$ km s^{-1}, with the majority of spaxels below 50 km s^{-1}. In the [N II]/Hα diagram in particular (Figure 2, left-hand panels) the average velocity dispersion increases with distance from the star-forming sequence. This result is generally consistent with the velocity dispersion mixing sequence presented by Ho et al. (2014) for a single disk galaxy observed by the SAMI survey, who similarly found that the lowest values of $\sigma_{\rm H\alpha}$ fell below the maximum-starburst line (see also the discussion by Kewley et al. 2001; Davies et al. 2016; D'Agostino et al. 2019). Indeed, given the kiloparsec-scale resolution of the MaNGA data, we should anticipate that each spaxel in practice likely contains gas excited by a range of different ionization mechanisms that would not be perfectly well differentiated. With the benefit of a 7000 times greater sample size, we can now much more clearly delineate the rapid increase in $\sigma_{\rm H\alpha}$ above the maximum-starburst line as radiative shocks and older stellar populations become increasingly contributors to the overall ionization of the gas.

In the [S II]/Hα and [O I]/Hα diagrams, we note that the use of these line ratios (with varying sensitivity to metallicity, temperature, ionization parameter, and other properties) results in little to no Intermediate sequence between the star-forming and AGN regions, however. Instead, the Intermediate sample is dominated by spaxels at lower $R3$ between the star-forming and LI(N)ER sequences, and many of the [N II]/Hα-identified Intermediate spaxels fall in the nominal star-forming region for [S II]/Hα and [O I]/Hα.

As illustrated by Figures 5 and 6, Intermediate region spaxels (selected via the [S II]/Hα diagram) are extremely similar to those in the star-forming population. In addition to only marginally larger gas and stellar velocity dispersions, they have similar radial distribution in galaxies of comparable stellar mass, a similar peak in D_n4000 (albeit with a larger tail to old stellar populations), and occur in galaxies with similar globally integrated Hα equivalent widths (again with an enhanced tail to the distribution). The most significant difference between the two populations is that the Intermediate population is systematically shifted to lower Hα equivalent widths for the individual spaxels.

Given the significant overlap in population distribution, properties, and dynamics with the star-forming sample, the evidence strongly suggests that these Intermediate spaxels may simply be those regions within ordinary star-forming disks that are either experiencing some degree of contributions from AGN/shocks or are dominated by older stellar populations with higher levels of diffuse ionized gas (DIG; a.k.a. the WIM) rather than gas in young H II regions. As discussed by Zhang et al. (2017), DIG-dominated regions with low star formation rate surface density (e.g., between spiral arms) can be shifted into this region of parameter space if hot evolved stars with hard spectral energy distributions contribute significantly to the ionizing photon budget.

Our dynamically defined Intermediate and LI(N)ER distributions may therefore simply represent DIG in actively star-forming and quiescent galaxies, respectively, with a continuous gradient between the two distributions in terms of their stellar population age, mass, and stellar/gaseous velocity dispersion. In predominantly star-forming galaxies, the contribution of DIG-like line emission shifts a given spaxel to larger $S2$ while having only a marginal effect on the line width because the disk stellar velocity dispersion is relatively small. Indeed, we note that both Bizyaev et al. (2017) and Levy et al. (2019) found a $\sim$1–2 kpc scale height for the DIG in edge-on galaxies from the MaNGA and CALIFA surveys, respectively, consistent with the observed asymmetric drift relative to the galactic H II regions. In predominantly quiescent galaxies the DIG-like line emission ratios are more extreme due to less residual contribution from H II regions, and the line widths are broader, reflecting the overall increase in the importance of pressure support to these evolved stellar systems. Such a picture is consistent with Figure 4 of Belfiore et al. (2016), who similarly found a significant increase in D_n4000 as a function of distance to higher $S2$ ratios from the Kewley et al. (2001) line.

4.4. Properties of the AGN Sequence

At larger values of $R3$, the AGN sequence is clearly distinguishable from both the star-forming and LI(N)ER sequences. Spaxels in this region are generally thought to have large forbidden line fluxes resulting from some combination of extended narrow-line region (ENLR) gas directly ionized by hard radiation from the central accretion disk (e.g., Groves et al. 2004; Kewley et al. 2013) and radiative shocks resulting

from the turbulent collision of feedback-driven gas flows with the surrounding interstellar medium (ISM; e.g., Allen et al. 2008; Rich et al. 2011).

As illustrated in Figures 5 and 6, the AGN sequence occupies an intermediate range of Hα equivalent widths (both in terms of individual spaxels and the galaxies in which those spaxels reside) and D_n4000 spectral break strengths characteristic of intermediate-age galaxies in the green valley and lower-SFR regions of the blue cloud. AGN-dominated spaxels are strongly biased toward smaller radii in higher host galaxy masses though, with typical radii $\sim 0.25R_e$ (albeit with a tail of the distribution extending above $1R_e$) and stellar mass $M_\odot \sim 10^{11}M_\odot$. The AGN/shock sequence thus has a similar mass distribution to the LI(N)ER sequence, but slightly younger stellar population ages and galaxy-integrated line emission more consistent with quenching late-type galaxies than with early-type galaxies.

In terms of their kinematics, AGN-dominated spaxels have a wide range of gas-phase velocity dispersions ranging from $\sigma_{H\alpha} = 50$–$200\,km\,s^{-1}$ or more.[20] Unlike LI(N)ERs the ratio between the gas-phase and stellar velocity dispersions in the AGN sample is commonly near unity (see also Ilha et al. 2019), with a significant number of spaxels exhibiting gas dispersions up to a factor of 2 in excess of the stellar velocity dispersion. At the lower end of this distribution, these velocities are consistent with ENLR gas directly illuminated by the accretion disk. At the upper end of the distribution, however, the gas is perhaps most likely to be shocked and not in dynamical equilibrium, as models suggest that the observed velocity dispersion of such gas should be consistent with the $\sim$100–$200\,km\,s^{-1}$ velocities of the shocks themselves (e.g., Rich et al. 2011). Intriguingly, Figure 5 suggests that AGN/shock-like spaxels at predominantly large versus small effective radii may be separable in terms of their typical *N*2 line ratio; however, this may simply reflect metallicity variations in the gas (e.g., Groves et al. 2004; Allen et al. 2008) rather than a distinction in the ionization source itself.

5. Sample-dependent Selection Effects

In Section 3 we defined our four broad populations based on a division of the [N II]/Hα, [S II]/Hα, and [O I]/Hα diagrams using the 1σ and 3σ limits of the clearly defined dynamically cold star-forming sequence. This division was based on the distribution of gas-phase velocity dispersions within the entire MaNGA galaxy sample, which is designed to be broadly representative of the $z = 0$ galaxy population (see Wake et al. 2017). However, as we explore here there are nonetheless a variety of both astrophysical and observational selection effects that are important to consider both within the MaNGA sample itself and when comparing to other samples.

5.1. Observational Selection Effects

In Figure 7 we repeat our earlier exercise from Figure 3, but focusing on the [S II]/Hα diagram and dividing the MaNGA spaxels into subsamples according to a variety of physical properties.

To start, we note a few properties that do not affect our conclusions. First, galaxy inclination (as derived from the NSA catalog) has only a marginal impact on the observed velocity dispersion trends, as subsamples with $i < 45°$ and $i > 45°$ both produce statistically identical distributions. If we break the galaxy sample into a greater number of bins (Figure 8) we note a marginal increase in velocity dispersion for star-forming spaxels in the most edge-on systems, consistent with the superposition of distinct velocity components along the line of sight. While this increase will be important for the study of individual galaxies, it has only a minor impact on the MaNGA ensemble result as 80% of our selected spaxels with $d_{S2} < 0$ lie in galaxies with $i < 60°$.

Second, the physical resolution of the MaNGA data does not appear to significantly affect our conclusions either. At the typical 2.″5 angular resolution of MaNGA, the effective spatial resolution of the data is about 2 kpc at the median redshift of the sample, and individual resolution elements will therefore be composed of gas ionized by a mixture of physical processes (e.g., AGN, H II regions, interarm DIG, etc.). We therefore compare results between the MaNGA Primary and Secondary samples,[21] which at median redshifts of 0.025 and 0.046 correspond to physical resolutions 1.3 and 2.3 kpc, respectively. Other than a small increase in the peak of the cold LOSVD from 24 to $27\,km\,s^{-1}$ (possibly due to an increase in the intraspaxel velocity gradient; see further discussion in D. Law et al. 2021, in preparation), there is no significant difference between the two, suggesting that our overall results are not a strongly varying function of spatial resolution.

In contrast, spaxels with higher S/N show a much sharper transition between entirely cold and entirely warm LOSVDs (i.e., a minimal Intermediate sequence) compared to spaxels in which Hα emission was detected at lower S/N. For the S/N < 50 subsample, the transition between populations occurs gradually over an Intermediate population of width 0.2–0.3 dex, while the S/N > 50 subsample jumps between an entirely cold LOSVD and an entirely warm LOSVD between adjacent bins with $-0.1 < d_{S2} < 0.0$ and $0.0 < d_{S2} < 0.1$ dex.

One possible explanation for this difference may be the larger uncertainties and known systematic bias of the low-S/N tail of the MaNGA sample to higher $\sigma_{H\alpha}$ due to the exclusion of spaxels whose observational uncertainties scatter them below the instrumental resolution (see discussion by Law et al. 2021, their Section 4.3). However, we do not believe this to be the primary explanation because even low-$\sigma_{H\alpha}$ spaxels in our low-S/N subsample in Figure 7 have a median Hα S/N = 36, for which uncertainties and biases are not substantially different than for the high-S/N subsample (Law et al. 2021, their Figure 15). Likewise, in the regions of parameter space where the median S/N is low (i.e., median S/N $\sim$ 20 in the traditional LI(N)ER region) the intrinsic velocity dispersion is high, and thus, systematic biases in measured $\sigma_{H\alpha}$ are negligible. Unsurprisingly, the primary effect of reconstructing Figure 2 using a more stringent threshold of S/N > 50 is thus to severely restrict the number of measurements in regions with weak overall Hα emission.

Rather, we believe the difference in the high- and low-S/N subsamples in Figure 7 to be due to the correlation between S/N and spaxel radius, in the sense that applying a more aggressive S/N > 50 cut systematically biases the observational sample to smaller radii, effectively downweighting the

[20] The MaNGA DAP is not designed to properly fit the extremely broad components characteristic of Type I AGNs (see Section 11 of Westfall et al. 2019), and these values are therefore incomplete at the highest values of $\sigma_{H\alpha}$.

[21] A simple redshift cut would impose a significant differential in stellar mass as well given the increase in stellar mass with redshift in the MaNGA sample (see Figure 1).

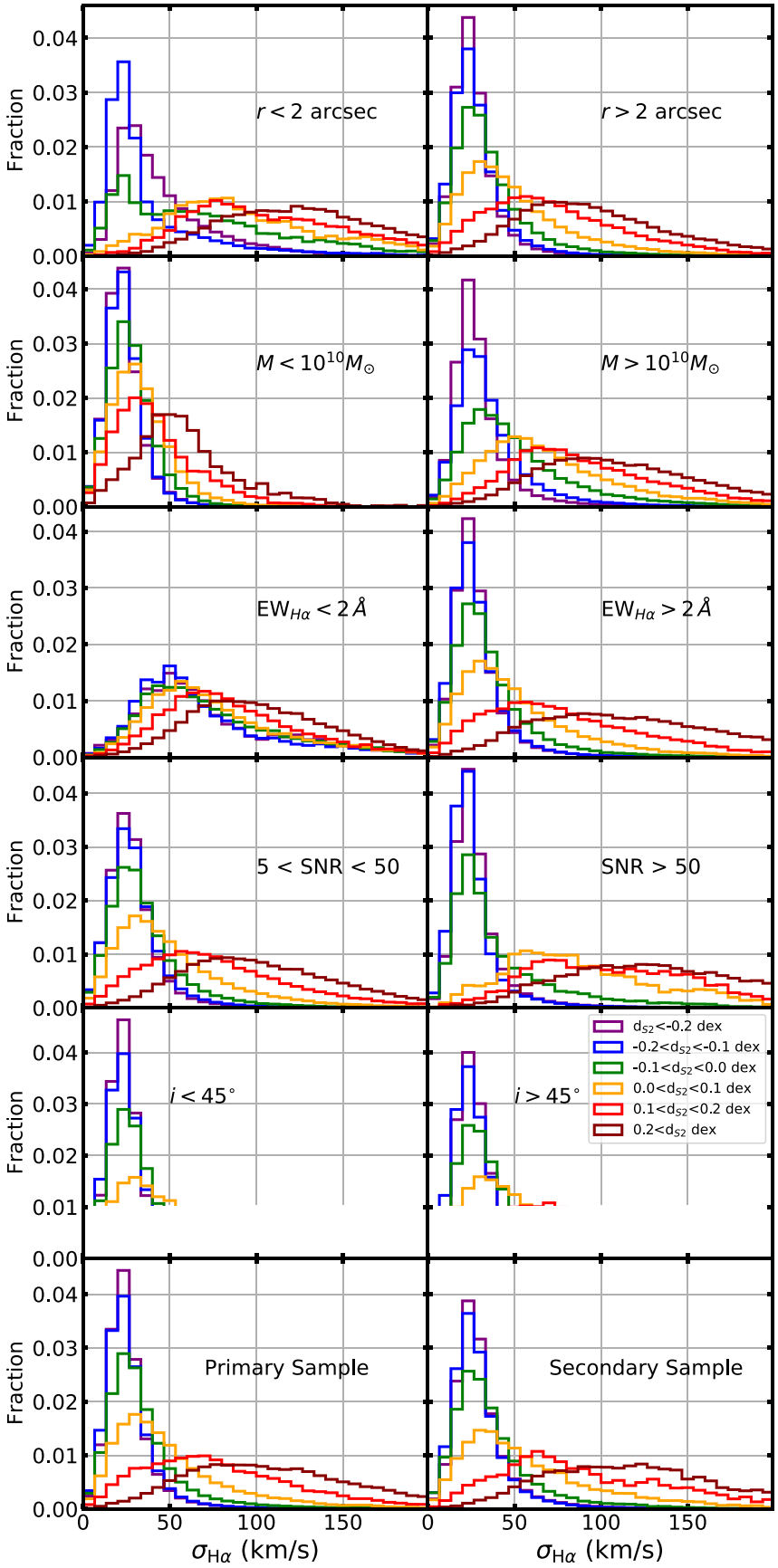

Figure 7. As Figure 3, but binned according to distance from our best-fit classification line in the [S II]/Hα diagram and split according to a variety of physical and observational parameters.

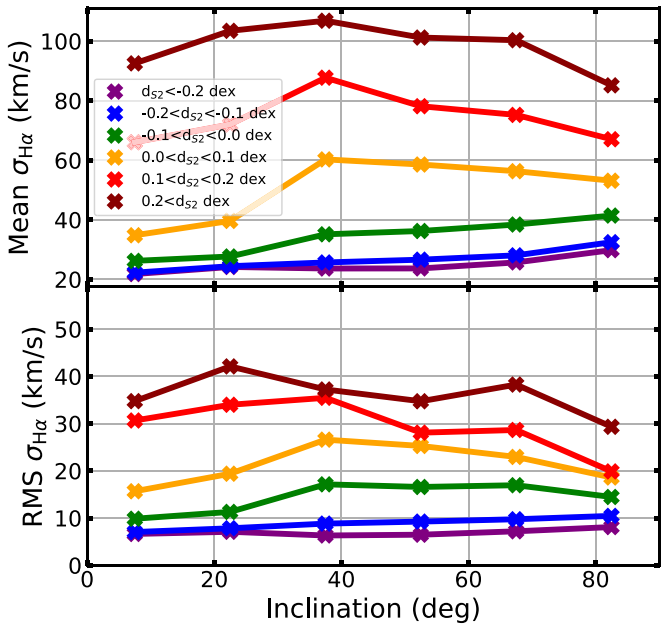

Figure 8. 2σ-clipped mean and rms velocity dispersion as a function of inclination for various bins of distance d_{S2} from our kinematically defined classification line in the [S II]/Hα vs. [O III]/Hβ space. Edge-on galaxies (90° inclination) show marginally larger velocity dispersions than face-on galaxies (0° inclination).

Intermediate sample compared to the AGN/LI(N)ER samples. Indeed, the sigma-clipped mean spaxel radius in the Intermediate region is 0.5 R_e when using an S/N > 50 cut, compared to 1.1 R_e when using an S/N > 5 cut (along with shifting to substantially older ages and higher masses). Surveys that are shallower than MaNGA (or that sample a different range of radii; see Section 5.4) would thus derive a different width for the Intermediate region, as may surveys that are substantially deeper.

5.2. Astrophysical Selection Effects

In terms of total galaxy mass, we note an appreciable difference between the low-mass and high-mass galaxy subsamples. As illustrated by Figure 7 (middle panels), galaxies of all masses show a similar dynamically cold LOSVD component corresponding to H II regions in the galactic thin disk. At low masses $M_* < 10^{10} M_\odot$, even spaxels in the AGN and LI(N)ER regions exhibit $\sigma_{H\alpha} < 100$ km s^{-1}. Likewise, spaxels in such low-mass galaxies are correspondingly skewed to younger ages and larger Hα equivalent widths, with stellar velocity dispersion profiles peaked around $\sigma_* = 60$ km s^{-1}. At larger masses $M_* > 10^{10} M_\odot$, however, the upper bound of the warm LOSVD gas increases to $\sim$200 km s^{-1} for the LI(N)ER and AGN samples, along with a corresponding increase in stellar population age and stellar velocity dispersion. This result is consistent with the deeper gravitational potential wells of higher-mass galaxies but more likely corresponds simply to the increasing prevalence of green-valley and red-sequence/early-type galaxies in the upper-mass end of the galaxy distribution. While the relatively flat mass distribution of the MaNGA sample in the range $M_* = 10^9$–$10^{11} M_\odot$ (see, e.g., Figure 6) has more high-mass galaxies than a purely volume-limited sample (see, e.g., Weigel et al. 2016), the addition of more low-mass galaxies would simply accentuate the dominance of the star-forming sample in an analysis of spaxels with detectable nebular line emission.

By far the most pronounced difference in gas LOSVDs is observed, however, if we compare galaxies whose Hα equivalent width is greater or less than 2 Å (which are found within the blue cloud and red sequence, respectively; see Figure 1). As illustrated by Figure 7, the gaseous LOSVD of spaxels with EW$_{H\alpha}$ > 2 Å broadly resembles the master spaxel sample with both cold and warm components. In contrast, there is no dynamically cold component to the LOSVD in spaxels selected with EW$_{H\alpha}$ < 2 Å; the 25 km s^{-1} galactic H II region signature is completely absent, even in cases where the emission-line flux ratios are nominally consistent with photo-ionization by young stars. Similarly, these spaxels live almost entirely in galaxies with stellar mass $\sim 10^{11} M_\odot$ and old stellar populations with strong 4000 Å breaks. Indeed, in such spaxels the LI(N)ER and Intermediate regions dominate the distribution, containing nearly six times more spaxels than the nominally star-forming region. The effectiveness of the EW$_{H\alpha}$ criterion in thus efficiently selecting LI(N)ER-type spaxels is in keeping with the prior findings of Yan et al. (2006), Cid Fernandes et al. (2010), Sánchez et al. (2012b, 2021), Belfiore et al. (2016), and Lacerda et al. (2018), who proposed using it as an additional classification axis beyond the usual [N II]/Hα, [S II]/Hα, and [O I]/Hα diagrams.

5.3. Analytical Selection Effects

As outlined in Section 2, we have used the versions of the MaNGA DAP data products that model the stellar continuum underneath the emission lines using hierarchically clustered sets of stellar spectra from the MaStar program (Yan et al. 2019), which used the MaNGA IFUs during bright time to observe a roughly 30,000 star stellar library using the same hardware and software as used to observe the MaNGA galaxies. As discussed in detail by Belfiore et al. (2019; see particularly their Figures 10 and 11), the choice of stellar continuum model used can have an impact on the recovered emission-line properties by altering the effective profiles of the Balmer absorption lines atop which emission is superposed.

In order to assess the impact of this template choice on our results, we repeated our analysis using a second set of DAP data products that instead used theoretical simple stellar population (SSP) models based upon the MaStar library (Maraston et al. 2020) that have systematically deeper Balmer line profiles. In the dynamically cold star-forming sequence, we find that the difference between the hierarchically clustered stellar spectra and the SSP models is inconsequential, with the SSP-derived velocities systematically larger by just 0.5 km s^{-1} (i.e., well within observational uncertainty). Unsurprisingly, the largest difference occurs in the LI(N)ER region of the emission-line diagnostic diagram, which is dominated by extremely low Hα equivalent widths. At fixed S/N selection criteria, the LI(N)ER region is significantly more well populated using the SSP models compared to the hierarchically clustered templates, adding about 150,000 new spaxels to those shown in Figure 2. These spaxels are located predominantly in high-mass ($M_* > 10^{11} M_\odot$) red-sequence galaxies and add about 700 such galaxies to the overall sample with emission-line regions meeting our S/N criteria. The addition of these extra spaxels does not change our overall conclusions but increases the median Hα velocity dispersion in the LI(N)ER region from 93 to 100 km s^{-1}.

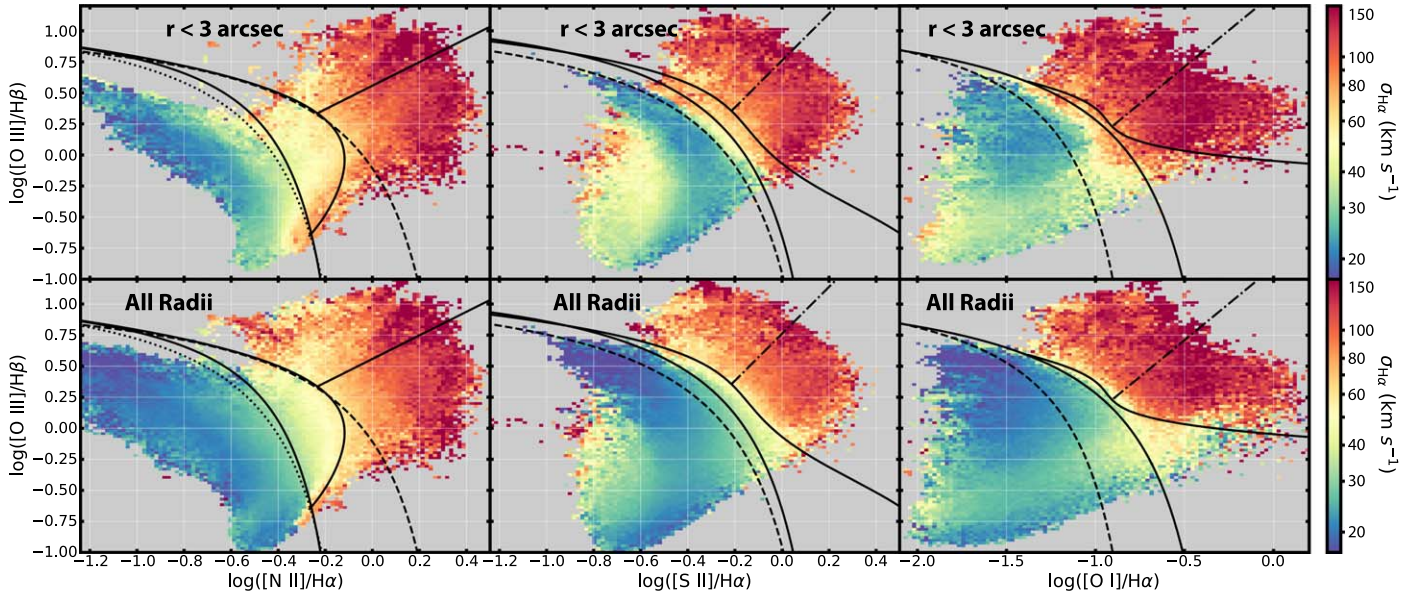

Figure 9. As in Figure 2 (lower panels), but comparing the results from the entire MaNGA spaxel sample (lower panels) against a subsample of spaxels from the central regions of galaxies chosen to closely mimic the selection effects of the original SDSS-1 spectroscopic survey (upper panels). Note the shrinking of the Intermediate region in the low-r subsample, along with a general shifting to lower line ratios of the warm LOSVD component.

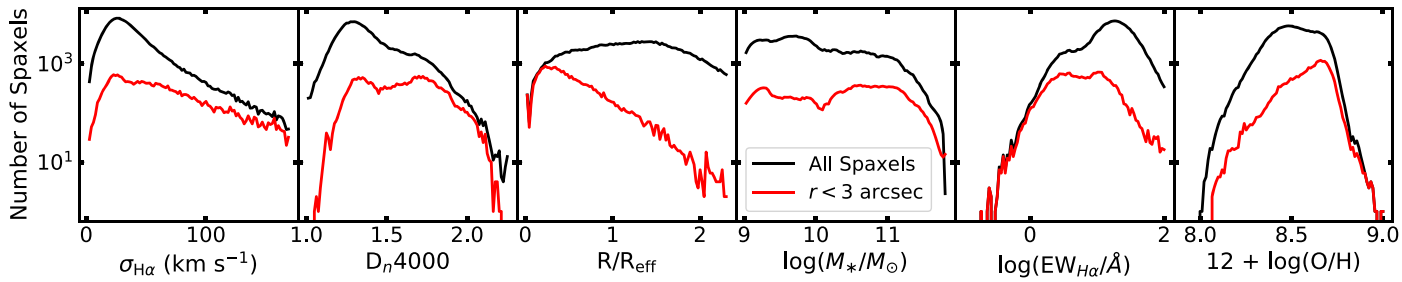

Figure 10. Histograms of the physical properties of spaxels with $S2$ and $R3$ line ratios placing them above the maximal-starburst relation of Kewley et al. (2001) but below the dynamical 1σ relation defined in Equation (2). Black and red histograms, respectively, illustrate the distribution for spaxels at all radii vs. spaxels with $r < 3''$ comparable to the regions that would have been contained within the original SDSS-I spectroscopic fiber apertures. The $r < 3''$ sample misses 93% of the stars in the parent sample, preferentially those with young ages and high Hα equivalent widths in low-mass galaxies.

5.4. Key Differences from the SDSS-I Sample

The radius-dependent selection effects described in the previous sections have significant implications for the comparison of our results to those based on the earlier-generation SDSS single-fiber spectroscopy (e.g., Kauffmann et al. 2003; Tremonti et al. 2004; Kewley et al. 2006; Stasińska et al. 2006). By virtue of the $3''$ diameter of the original SDSS-I spectroscopic fibers, that sample was subject to a severe radial selection bias compared to the integral-field SDSS-IV/MaNGA observations.

The Kauffmann et al. (2003), Tremonti et al. (2004), and Stasińska et al. (2006) samples for instance consisted of about 123,000, 53,000, and 20,000 galaxy spectra, respectively, with a median redshift $z \approx 0.1$ at which the SDSS fiber subtended a radius of about 3 kpc. Similarly, the Kewley et al. (2006) sample contained 85,000 galaxies in the redshift range $z = 0.04$–0.1, for which the SDSS fiber subtended a radius of 1–3 kpc. In contrast, the SDSS-IV MaNGA sample is both significantly larger (~300,000 statistically independent spectral samples with $> 5\sigma$ emission-line detections; see Section 3) and covers a much larger radial extent of 9 kpc on average at the median redshift $z = 0.04$.

We assess the impact of this bias on the SDSS-I sample by applying an $r < 3''$ cut to the MaNGA data.[22] As illustrated in Figure 9, the median gas velocity dispersion as a function of strong line intensity ratios changes enormously with such a radial cut. Compared to the full MaNGA sample, the restricted central radial range loses a large fraction of the cold-disk sequence, shrinks the Intermediate population to produce a much sharper division between cold and warm LOSVDs, and shifts the warm LOSVD population toward the lower left in the [N II]/Hα, [S II]/Hα, and [O I]/Hα diagrams. For instance, we note that while the [S II]/Hα and [O I]/Hα relations of Kewley et al. (2001, dashed line in Figure 9, middle and right panels) underpredict the range of the cold LOSVD population when considering all MaNGA spaxels, they do a much better job of matching the dynamical dividing line when considering only spaxels at $r < 3''$.

As we show in Figure 10 this is because the SDSS-I radial selection function misses a statistically important sample of high Hα equivalent width spaxels in regions with young stellar populations. In the full MaNGA sample these spaxels dominate

[22] $r < 3''$ at the median redshift of the MaNGA sample corresponds nearly to $r < 1\farcs5$ at $z = 0.1$; the Kewley et al. (2006) sample radial cut is thus even more restrictive than we model here.

the region in the [S II]/Hα and [O I]/Hα diagrams above the Kewley et al. (2001) relation but below our dynamical 1σ relation given in Equation (2). Because they are primarily located at larger radii $\sim 0.5-2R_e$ these spaxels are almost entirely absent from the SDSS-I sample.

Given the strong radial concentration of the AGN and LI(N)ER samples (Figure 7) a radial selection bias at the same time artificially increases the numerical significance of these two populations relative to the star-forming and intermediate samples. As illustrated by Figure 10 an SDSS-I-like radial cut includes nearly all of the high-D_n4000, low-$EW_{H\alpha}$, high-$\sigma_{H\alpha}$ spaxels in the full MaNGA sample while undercounting the low-D_n4000, high-$EW_{H\alpha}$, low-$\sigma_{H\alpha}$ spaxels by nearly two orders of magnitude.[23]

These differences are not limited to the narrow region above the [S II]/Hα line of Kewley et al. (2001). Using the *O3N2* metallicity relation defined by Pettini & Pagel (2004),

$$12 + \log(\mathrm{O/H}) = 8.73\text{–}0.32 \times (R3 - N2), \quad (10)$$

we find that the full MaNGA spaxel sample in the dynamically cold 1σ region is more metal poor than the $r < 3''$ subsample of the MaNGA data. The shift in the median value from $12 + \log(\mathrm{O/H}) = 8.69$ to 8.63 dex is driven by the increased prevalence of spaxels with $12 + \log(\mathrm{O/H}) \sim 8.5$ dex at large radii (see also Sánchez et al. 2014), which has significant implications for the construction of photoionization models (as we discuss further in Section 6).

In a spatially resolved sense, these differences are clearly of interest both for what they tell us about the extended structure of galaxies and for their implications for stellar photoionization models (see discussion in Section 6). In an integrated sense, however, their significance is more ambiguous because the total galaxy light tends to be dominated by the central regions. Indeed, if we compute the Hα flux-weighted mean velocity dispersion in each bin in Figure 9 instead of the sigma-clipped mean (which is effectively an area weighting), we find very little difference between the low-radius and all-radius subsamples because the low-radius points dominate in both cases.

In either sense, however, caution is warranted when applying line ratio selection criteria derived from central spaxels in the low-redshift universe to identify star-forming regions in the distant universe. Unlike the SDSS-I $z = 0$ sample, seeing-limited studies at higher redshifts tend to include a much larger fraction of the galaxy in the optical slit, all of which may have stellar populations that are substantially younger and of lower metallicity than typically found in the central regions of nearby galaxies. Likewise, adaptive-optics-fed IFU studies at high redshift (e.g., Law et al. 2009; Förster Schreiber et al. 2018, and references therein) typically resolve the galaxy emission with a comparable kiloparsec-scale resolution to MaNGA. The offsets in median metallicity and the upper envelope of the star-forming sequence between the low- and high-radius subsamples of MaNGA data are thus potentially significant compared to the observed offset in the mass–metallicity relation between the $z = 0$ sample and galaxy populations at higher redshifts (e.g., Erb et al. 2006; Maiolino et al. 2008; Sanders et al. 2020). Although the majority of this offset appears to be due to intrinsic physical differences between the galaxy populations (e.g., a harder stellar ionizing spectrum at fixed nebular metallicity due to alpha enhancement; Steidel et al. 2016; Strom et al. 2017; Topping et al. 2020), the systematic underrepresentation of low-metallicity regions in the SDSS single-fiber comparison sample should not be ignored.

[23] Belfiore et al. (2016) similarly remarked upon this effect, noting both the extension above the Kewley et al. (2001) demarcation line in the [S II]/Hα BPT diagram of MaNGA star-forming spaxels and the virtual absence of the large population of intermediate-D_n4000 LI(N)ER-like spaxels in SDSS.

6. Comparison to Theoretical Models

Photoionization models have been used by several authors to constrain the position of H II regions (and therefore star-forming galaxies) in the BPT diagram. Kewley et al. (2001) presented the first set of easily applicable demarcation lines in the BPT diagram based on modern ionizing continuum models. In detail, Kewley et al. (2001) present models computed using the Mappings III photoionization code (Binette et al. 1985; Sutherland & Dopita 1993) and using ionizing spectra from two different spectral synthesis codes, Starburst99 (Leitherer et al. 1999) and Pegase 2 (Fioc & Rocca-Volmerange 1997). The locations of the H II regions in the BPT diagrams predicted by these two sets of models are remarkably different. Kewley et al. (2001) argued in favor of the PEGASE 2 models, because of their harder extreme ultraviolet (EUV) slope, which provided a better fit to observations of a small sample of starburst galaxies then available. These PEGASE 2 Kewley et al. (2001) models are shown in the first row of Figure 11. Each colored line represents a set of models with the same metallicity, spanning a range of ionization parameters, which in the BPT planes decreases going from the top left to the bottom right. The characteristic "folding over" of the models in the BPT planes generates a well-defined envelope for star-forming models, which is fitted by the Kewley et al. (2001) demarcation lines (dashed black lines in the figure).

The success of the predictions of Kewley et al. (2001) using the PEGASE 2 models in the [S II]/Hα and [O I]/Hα BPT diagrams have been clearly demonstrated by Kauffmann et al. (2003), who compared them with line ratio measurements from early SDSS fiber spectroscopy. The excellent fit to these observations provided by the Kewley et al. (2001) demarcation lines in the [S II]/Hα and [O I]/Hα BPT diagrams has cemented the use of these boundaries in subsequent works.

The Kewley et al. (2001) models did not provide an equally good representation of the envelope of star-forming galaxies in the [N II]/Hα BPT diagram. This prompted Kauffmann et al. (2003) to define an empirical demarcation line in the [N II]/Hα diagram (black dotted–dashed curve in Figure 11) to replace the Kewley et al. (2001) predictions. The subsequent denomination of the region between the Kewley et al. (2001) and Kauffmann et al. (2003) lines in the [N II]/Hα diagram as "intermediate" has regrettably contributed to the continued use of the incorrect [N II]/Hα Kewley et al. (2001) demarcation line, despite the progress made by subsequent authors to build models that more accurately match the empirical Kauffmann et al. (2003) line.

Levesque et al. (2010) expand on the work of Kewley et al. (2001) by using STARBURST99 with the newer Pauldrach et al. (2001) and Hillier & Miller (1998) atmospheres, which include continuum metal opacities. They compute photoionization models with an updated version of MAPPINGS, which includes a more sophisticated treatment of dust (Groves et al. 2004). In Figure 11 we show the position in the BPT planes of their models calculated using the "high" mass-loss tracks, a constant star formation history (SFH), a Salpeter initial mass function (IMF) with a 100 $M_\odot$ upper cutoff, and an age of

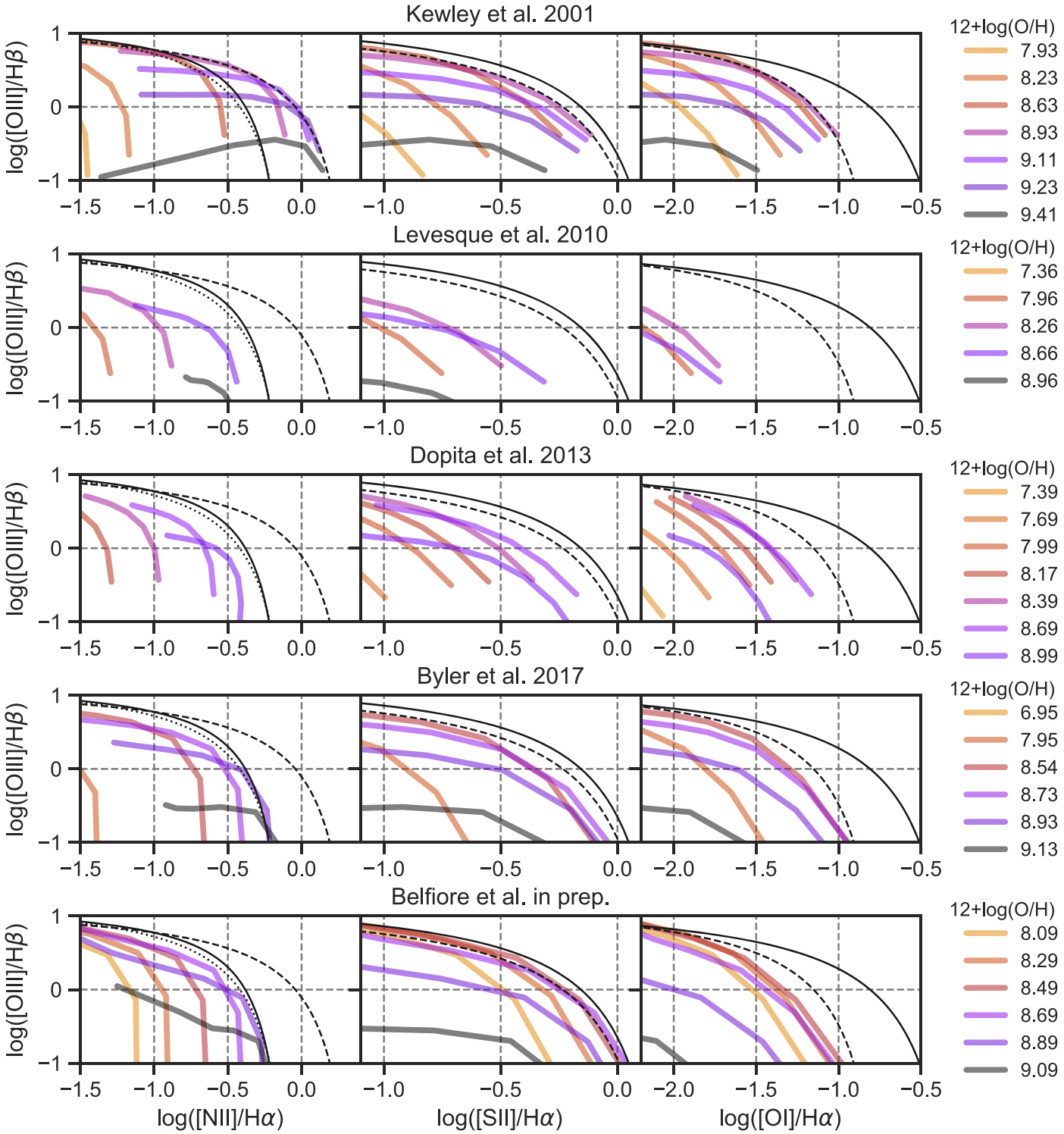

Figure 11. Photoionization model predictions from the literature in the [N II]/Hα [S II]/Hα and [O I]/Hα BPT diagrams. Each row presents sets of models taken from the papers cited in the figure. In each panel, the colored lines are models computed for a fixed oxygen abundance (given in the legend) and a range of ionization parameters. Log U generally decreases from the top left to the bottom right in all BPT planes, and models by different authors cover different ranges and values of log U. The black lines represent proposed demarcation lines for star-forming galaxies. The dashed lines are from Kewley et al. (2001) and were proposed as a representation of the envelope of their models shown in the topmost row. The dotted line is the empirical demarcation line from Kauffmann et al. (2003) for the [N II]/Hα diagram. The solid lines are the 1σ demarcation lines presented in this work (Equations (1)–(3)). The recent models by F. Belfiore et al. (2021, in preparation) present an excellent fit to the demarcation lines proposed in this work in the [N II]/Hα and [S II]/Hα BPT diagrams. No set of models in the literature is capable of reproducing the new proposed demarcation line in the [O I]/Hα BPT.

6 Myr. Despite the important theoretical improvements, the position of these models is close to that of the STARBURST99 models computed by Kewley et al. (2001; not shown) but substantially offset with respect to the PEGASE 2 Kewley et al. (2001) models. In detail, in the [N II]/Hα diagram the envelope of the Levesque et al. (2010) models is shifted to the lower left,

providing a poor fit to the observational data, but in the opposite sense to the Kewley et al. (2001) demarcation line. The envelopes in the [S II]/Hα and [O I]/Hα diagrams are also offset to the bottom left of the plane with respect to the data, producing an overall much worse fit to both the SDSS single-fiber observations and the MaNGA results presented in Section 3 than the original Kewley et al. (2001) models.

Dopita et al. (2013) present models with an upgraded version of MAPPINGS (IV), but using the older STARBURST99 atmospheres also employed in Kewley et al. (2001; in part to avoid the issues presented in Levesque et al. 2010, who used the newer atmospheres). The Dopita et al. (2013) models come substantially closer to the envelopes of the observational data in all BPT diagrams. In Figure 11 we show the models with a constant SFH, an age of 4 Myr, and a Salpeter IMF (and adopting the canonical Maxwell–Boltzmann distribution of electron energies). While Dopita et al. (2013) compute models with metallicity $12+\log(\mathrm{O/H}) > 9.0$, such models occupy an unphysical area of the BPT diagram to the far bottom left outside the plot area presented in the figure.

Byler et al. (2017) present models based on modern stellar atmospheres for hot stars and simple stellar population models generated by FSPS (Conroy et al. 2009). In particular, FSPS makes use of O- and B-star spectra generated with WMBasic (Pauldrach et al. 2001), while Wolf–Rayet stars are taken from the spectral library of Smith et al. (2002). Their model simple stellar populations are computed with both Padova (Marigo et al. 2008) and MIST (Choi et al. 2016; Dotter 2016) isochrones. All models are computed with the photoionization code CLOUDY v13.03 (Ferland et al. 2013). In Figure 11 we show the Padova models for a 1 Myr SSP. Considering that this work makes use of modern stellar atmospheres, they have largely improved on Levesque et al. (2010) by coming substantially closer to all BPT demarcation lines (although code differences, dust depletion factors, and relative abundance prescriptions will also have an effect). Moreover, unlike the original Kewley et al. (2001) models, they correctly reproduce the Kauffmann et al. (2003) demarcation line in the [N II]/Hα diagram. The MIST isochrone models (not shown) provide an equally good match but continue to match the data for older ages, thanks to the inclusion of stellar rotation.

The most recent update of the CLOUDY code (v17; Ferland et al. 2017) includes a change in the dielectronic recombination coefficient for S^{++} (Badnell et al. 2015), which was previously unknown, and estimated by the charge-normalized mean dielectronic recombination rates for C, N, and O (Ali et al. 1991). Given the importance of the dielectronic recombination channel for S^{++} in nebular conditions, the update caused an increase in the predicted flux of the [S II] lines. F. Belfiore et al. (2021, in preparation) recomputed models based on the same formalism as Byler et al. (2017), but with this updated CLOUDY version. In the last row of Figure 11 we show models computed using the same input physics as Byler et al. (2017), MIST isochrones, and age of 2 Myr. The only significant change with respect to the previous Byler et al. (2017) models is in the [S II]/Hα BPT diagram, where the new models lie above the Kewley et al. (2001) demarcation line. However, as we demonstrated in Figure 10 this is precisely the region in which MaNGA data show evidence for a substantial population of young, high-equivalent-width and low-metallicity spaxels whose large radii meant that they were missed by the original SDSS fiber spectroscopy against which the Kewley et al. (2001) models are traditionally compared. In contrast, the new models of F. Belfiore et al. (2021, in preparation) almost exactly match our new dynamical boundary to the star-forming sequence defined in Section 3 (black solid lines in Figure 11). In summary, modern photoionization models are capable of reproducing the demarcation lines of Kauffmann et al. (2003) (or the nearly identical kinematically defined line proposed here) in the [N II]/Hα diagram, while the Kewley et al. (2001) line in this diagram should no longer be used. Recent updates to the atomic data for S^{++} lead to model predictions that follow the [S II]/Hα demarcation line proposed in this work almost exactly.

In contrast, no set of models presented in the literature extends to the right of the Kewley et al. (2001) line in the [O I]/Hα diagram, and the MaNGA spaxels in this range whose gas-phase velocity dispersions are consistent with H II regions in thin disks are therefore not currently reproducible theoretically. In part, this may be because contamination from DIG can affect the observed line ratios in low-surface-brightness regions probed by MaNGA and contribute (at least partially) to their higher *O*1. While *N*2 and *S*2 are also enhanced in the DIG with respect to H II regions, the effect is of the order of 0.4 dex, while for *O*1 the DIG show higher line ratios by up to 1.2 dex (Zhang et al. 2017), therefore constituting a much more severe contaminant. However, as we demonstrated in Section 5.4, the spaxels in this region generally have large Hα equivalent widths unlike those observed from DIG. At the same time, the [O I] line emission is notoriously difficult to model accurately (see discussion by X. Ji et al. 2021, in preparation) because it is produced in the narrow partially ionized zone at the boundary between H II regions and neutral clouds, and it is strongly affected by the presence of shocks or DIG. The relative role of young star-forming regions and contributions from DIG to line ratios measured on kiloparsec scales therefore remains an active area of research and needs to be assessed with higher spatial resolution observations of nearby star-forming galaxies (F. Belfiore et al. 2021, in preparation).

Another complicating factor is that the definition of a "best-fit" photoionization model is itself ambiguous. In the discussion above we have assumed that the envelopes of the ideal photoionization models should match exactly the 1σ dynamical demarcation lines observed in Figure 2 to within some uncertainty associated with variations in secondary model parameters (e.g., stellar SEDs, dust depletion factors, prescriptions for secondary elements, etc.) in the observed H II regions. However, as suggested by Ji & Yan (2020), from a statistical point of view, the most representative photoionization model found in a multidimensional line ratio space would not necessarily match the demarcation lines in any given two-dimensional projection of that space. To better evaluate the goodness of fit, it is thus important to check the consistency of model predictions across multiple emission-line ratios (see, e.g., Vogt et al. 2014; Mingozzi et al. 2020).

7. Separating Different Kinematic Components in a Three-dimensional Line Ratio Space

A consistency check reveals that of 3.2 million spaxels that satisfy either our [N II]/Hα or [S II]/Hα star-forming selection criteria,[24] 88% simultaneously satisfy both selection criteria, 11% are indicated to be star-forming using the [S II] selection

[24] Applying a consistent 5σ S/N requirement on both [N II] and [S II].

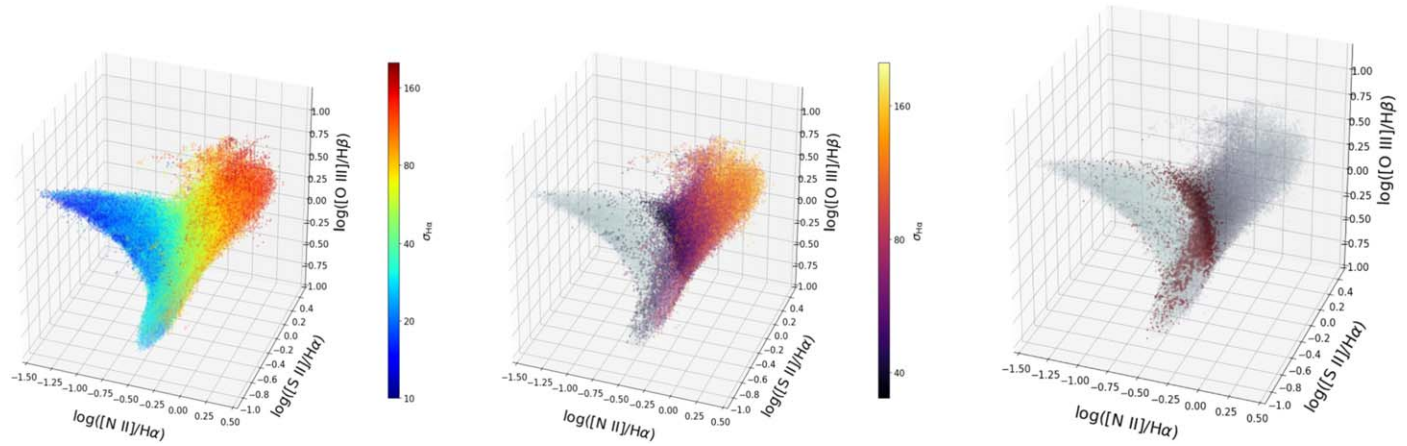

Figure 12. Left: 3D BPT diagram viewed at an elevation angle of 30°. Data are binned in the 3D line ratio space, and the bins are color-coded according to their sigma-clipped mean $\sigma_{\rm H\alpha}$ values. While a total of $75 \times 75 \times 75$ bins are constructed, only bins made up of a minimum number of 5 spaxels are shown. A 3 s animation of this figure panel is available that shows a rotation of the displayed points around the vertical axis. Middle: bins with $\sigma_{\rm H\alpha} < 35$ km s^{-1} are made transparent and only bins with $\sigma_{\rm H\alpha} > 35$ km s^{-1} are color-coded. Right: bins with $\sigma_{\rm H\alpha} = 33$–$37$ km s^{-1} are shown in red, of which the displayed sizes are set to be proportional to the number of spaxels inside the bins. The rest of the bins are made transparent.

(An animation of this figure is available.)

Table 1
Purity and Completeness of Spaxel Selection Techniques

Method	Purity	Completeness
N2–R3	83%	95%
S2–R3	77%	99%
O1–R3	75%	99%
P_1–P_2	83%	96%

but not the [N II] selection, and 1% are indicated to be star-forming using the [N II] selection but not the [S II] selection. The major reason for differences between the [N II] and [S II] selection techniques is thus the relatively large fraction of spaxels indicated to be star-forming by the [S II] technique but not the [N II], 86% of which fall within the Intermediate classification region for the [N II] diagram. The median velocity dispersion of this latter population is 47 km s^{-1} (i.e., substantially larger than the 24 km s^{-1} median for spaxels for which the [N II] and [S II] techniques agree upon a star-forming classification), suggesting that the [S II] technique incorporates a relatively large fraction of spaxels that are not dynamically cold. Features like the "*S*2 bump" in the *S*2–*R*3 diagram are mainly composed of such misclassified spaxels.

If we instead define star-forming spaxels to be those with dynamically cold Hα velocity dispersions $\sigma_{\rm H\alpha} < 35$ km s^{-1}, we can calculate both the purity (i.e., the fraction of spaxels meeting a given line ratio selection criterion that are dynamically cold) and the completeness (i.e., the fraction of dynamically cold spaxels that meet a given line ratio selection criterion) of all three [N II], [S II], and [O I] selection techniques.[25] As indicated by Table 1, the *N*2–*R*3 method has better selection purity than the *S*2–*R*3 or *O*1–*R*3 methods, but lower completeness.

[25] This approach will be limited by our appreciable uncertainties on individual spaxel velocity dispersions and by the questionable validity of our assumption that dynamically cold velocity dispersions are necessarily and uniquely star-forming. However, it nonetheless provides a convenient numerical point of comparison.

Recently, Ji & Yan (2020) proposed using a 3D diagnostic diagram composed of *N*2, *S*2, and *R*3 to obtain a cleaner separation of different ionization mechanisms and found that the photoionization models (which are 2D surfaces with varying metallicity and ionization parameter) that represent H II regions and AGN regions are well separated in both 3D and in carefully chosen reprojections of this space. Using velocity dispersion as a proxy for "true" star-forming spaxels, we explore whether a similar reprojection can better highlight the separation between star-forming and non-star-forming spaxels than the traditional axes.

In Figure 12, we plot the distribution of our data in a 3D line ratio space spanned by *N*2, *S*2, and *R*3. The data points are binned in this 3D space, and the color-coding shows the sigma-clipped mean $\sigma_{\rm H\alpha}$ of the spaxels inside each bin. The left panel shows a clear color gradient in the data distribution, where $\sigma_{\rm H\alpha}$ increases from the star-forming (SF) locus to the AGN region. We note that the high $\sigma_{\rm H\alpha}$ bins continuously extend to low *S*2 values. When projected to two dimensions (e.g., Figure 2), the high-$\sigma_{\rm H\alpha}$ spaxels that overlap with the main star-forming cold-dispersion sequence are not numerous enough to significantly affect the average. At the low *S*2 end of the distribution, however, there are substantially fewer cold star-forming spaxels, and the high-$\sigma_{\rm H\alpha}$ spaxels therefore give rise to what appears to be an isolated "*S*2 bump" in the average velocity dispersion and stellar population properties around $S2 = -0.8$ and $R3 = 0$. From a 3D point of view, at high metallicity the [N II]/Hα BPT diagram is thus a cleaner projection that better conserves the gradient of the gas velocity dispersion. This arises because the photoionization model surface that describes the SF region is more edge-on in the [N II]/Hα diagram at high metallicity and more face-on in the [S II]/Hα diagram. As a result, the composite regions with high metallicities are able to extend further below the demarcation line in the [S II]/Hα diagram. Although it is less obvious in the [N II]/Hα diagram, we also see spaxels of relatively high $\sigma_{\rm H\alpha}$ below the demarcation line. Therefore, we want to find a kinematically defined dividing surface in 3D that better isolates the dynamically cold component. With such a surface, we can further construct a 2D projection that minimizes the projected

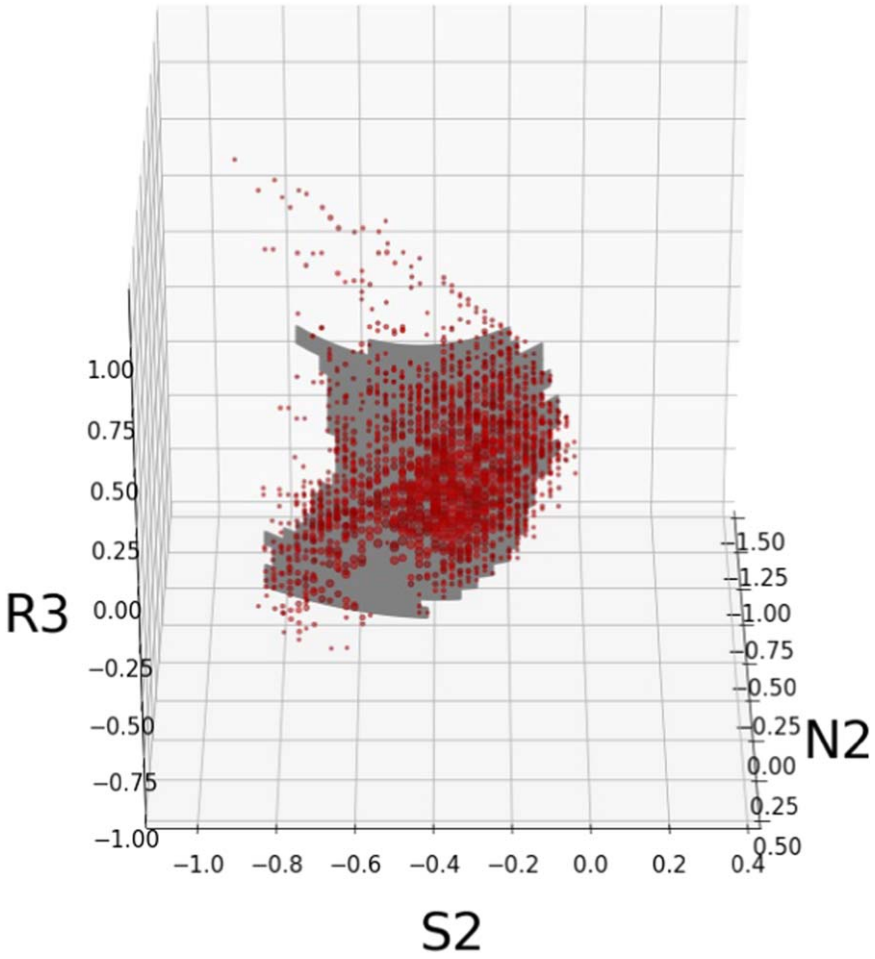

Figure 13. Polynomial surface (gray) that fits the 3D bins (red) used to define the dividing surface for the cold and warm kinematic components. The polynomial surface is cut so that only the part that covers the middle 99% of the data along all three axes remains. The displayed sizes of the bins are scaled according to the number of spaxels they contain.

area of the surface. This projection will help us visualize the separation of different kinematic components.

In Section 3, we used groups of spaxels offset in line ratio space from the Kauffmann et al. (2003) relation to define a dynamically cold sample of spaxels and found that the 1σ upper boundary on this sample lay at about 35 km s^{-1}. We now perform a similar calculation in 3D, computing the velocity dispersion as a function of the 3D distance from the star-forming photoionization model reference surface presented by Ji & Yan (2020).[26] Once again, we find that the 1σ wing of the cold LOSVD is roughly 35 km s^{-1}; the middle and right panels of Figure 12 show the locations of the 3D bins with $\sigma_{\mathrm{H}\alpha} \sim 35$ km s^{-1} and the regions they separate in 3D.

By analogy to our approach in 2D, we then use an analytical function of the form

$$N2 = \sum_{i=0}^{2} \sum_{j=0}^{2} C_{ij} S2^i R3^j \tag{11}$$

to trace the 35 km s^{-1} isodispersion surface in 3D. In detail, we use a fast least trimmed squares algorithm to fit 3D bins with $33\ \mathrm{km\ s^{-1}} < \sigma_{\mathrm{H}\alpha} < 37\ \mathrm{km\ s^{-1}}$ so as to minimize the influence of outliers (Rousseeuw & van Driessen 2006; Cappellari et al. 2013).

[26] As before with the Kauffmann et al. (2003) relation, our results do not depend strongly on the choice of the model grid so long as it provides a reasonable match to the overall shape of the star-forming region.

Table 2
Coefficients of the Polynomial Surface

C_{ij}	$j = 0$	1	2
$i = 0$	−0.7362	−0.6464	−0.3036
1	−1.7567	−1.2338	0.4533
2	−2.0170	−1.3520	0.3177

To better reflect the distribution of the observed data in 3D, we only fit the part of the surface that continuously covers the middle 99% of the 3D bins along all three axes (we additionally ensure that the surface behaves well when it is extrapolated outside the region covered by the MaNGA data). The final coefficients of this polynomial surface are given in Table 2 and illustrated in Figure 13.

Following Ji & Yan (2020), we next look for the viewing angles that make this 3D surface appear closest to edge-on by minimizing its projected 2D area along different lines of sight. Each line of sight is described by the polar angle θ and the azimuthal angle ϕ (in the right-handed coordinate system $N2$–$S2$–$R3$ shown in Figure 14, so that θ is defined relative to the positive direction of $R3$, and ϕ is defined relative to the positive direction of $N2$). We vary θ from 0° to 180° and ϕ from 0° to

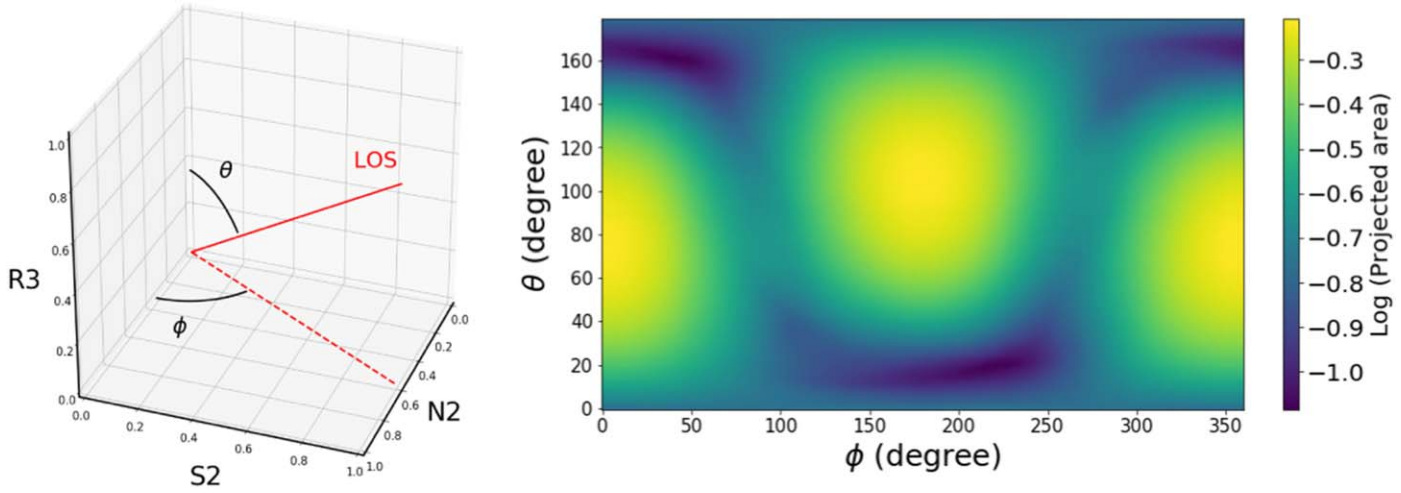

Figure 14. Left panel: definition of the viewing angles in the 3D space. Right panel: logarithm of the projected area of the polynomial dividing surface as a function of the two viewing angles in 3D. The two degenerate global minima occur at $(\theta, \phi) = (19^\circ, 215^\circ)$ and $(\theta, \phi) = (161^\circ, 35^\circ)$.

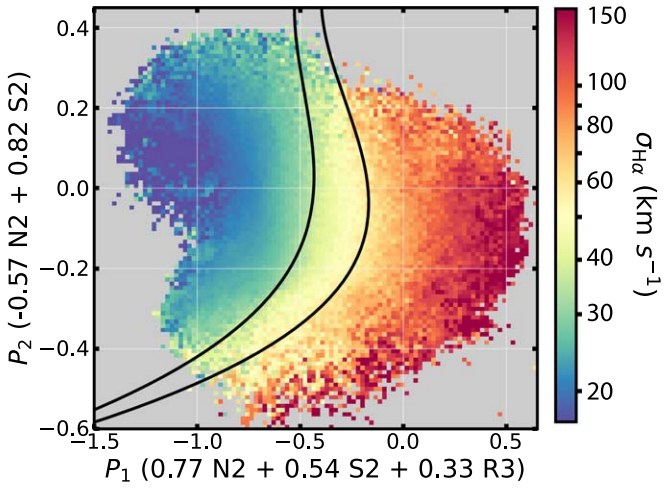

Figure 15. Sigma-clipped mean Hα velocity dispersion of the MaNGA spaxels in our kinematically defined P_1−P_2 line ratio space that makes the 3D isodispersion surface closest to edge on.

360° in increments of 1°. The results are shown in Figure 14 and indicate a clear valley of minima indicating the rotational symmetry of the polynomial surface. The global minima lie at $(\theta, \phi) = (19^\circ, 215^\circ)$ and the rotationally degenerate point $(\theta, \phi) = (161^\circ, 35^\circ)$ which specifies the same viewing axis with the opposite sign. Figure 15 shows the 2D projection corresponding to $(\theta, \phi) = (19^\circ, 215^\circ)$. Because we have rotational freedom about the viewing axis, we choose the vertical axis of the projection, P_2, to be linear combinations of $N2$ and $S2$, while the horizontal axis, P_1, is a linear combination of $N2$, $S2$, and $R3$. These projections are given by

$$P_1 = 0.77N2 + 0.54S2 + 0.33R3 \quad (12)$$

and

$$P_2 = -0.57N2 + 0.82S2. \quad (13)$$

As illustrated in Figure 16 the 3D polynomial isodispersion surface is almost face on in the $S2$−$R3$ diagram, corresponding to a large fraction of spaxels with high $\sigma_{H\alpha}$ (i.e., the "$S2$ bump") that are mixed with the dynamically cold component. In the $N2$−$R3$ diagram, the outer envelope of the 3D surface is well reproduced by our 1σ demarcation line. Nonetheless, the surface still partly extends to the left of this demarcation line, and as a result, there will be some fraction of spaxels misclassified as the cold-disk component in the $N2$−$R3$ diagram as well. In contrast, the 3D surface has the narrowest projection of all in our kinematically defined P_1−P_2 frame, overlapping very little with the H II regions on the left-hand side of the figure.

In Figure 15, we plot the sigma-clipped mean $\sigma_{H\alpha}$ of our data in this projection. The mean velocity dispersion shows a regular well-defined gradient, and we follow Section 3 in deriving corresponding relations that bound the 1σ and 3σ limits of the cold-disk sequence as

$$P_1 = 2.597P_2^3 - 1.865P_2^2 + 0.105P_2 - 0.435 \quad (14)$$

and

$$P_1 = 3.4P_2^3 - 2.233P_2^2 - 0.184P_2 - 0.172. \quad (15)$$

As detailed in Table 1, we find that the corresponding dynamically cold purity of the spaxels selected in such a manner is 83%, with a completeness of 96%. The P_1−P_2 selection method is therefore comparable to the $N2$−$R3$ method in terms of completeness, while both have significantly better purity than the $S2$−$R3$ and $O1$−$R3$ methods.

We note that this "best" kinematic projection is not uniquely defined considering the uncertainties associated with the derivation, and other projections with the line of sight near the local minima shown in Figure 14 might give equally good results. Similarly, it differs by about 20° from the best projection angle derived by Ji & Yan (2020) using theoretical photoionization models. One explanation for this difference may be that Ji & Yan (2020) defined their projection as the common normal plane of two representative patches on their SF-ionized model and AGN-ionized model, which effectively minimizes the projected areas of both of their model surfaces at the same time. The result might be different if only the SF-ionized model was considered. Alternatively, if we had chosen a value other than $\sigma_{H\alpha} = 35$ km s^{-1} for defining the isodispersion surface, we would have plausibly derived a different optimal projection. Likewise, the photoionization models used by Ji & Yan (2020) may need to be improved as the model-based surface may have difficulty accurately describing very

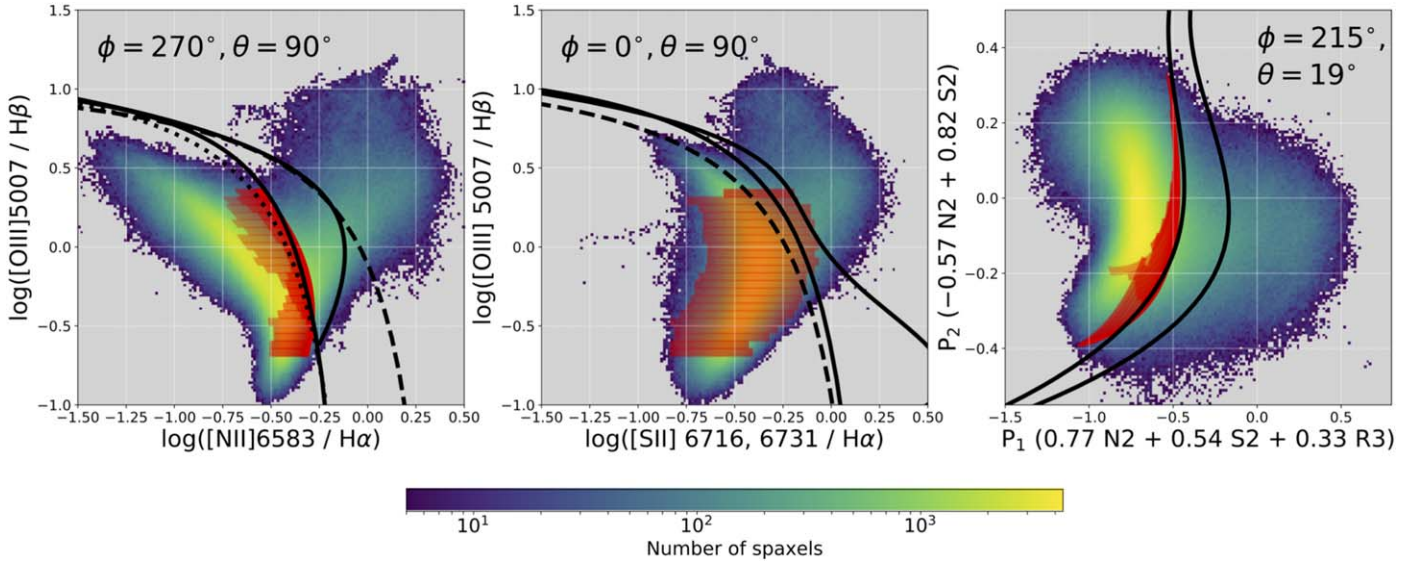

Figure 16. Density distributions of MaNGA spaxels in different projections of the three-dimensional line ratio space. The polar coordinates (ϕ, θ) are used to define the viewing angle, where ϕ is the angle with respect to the positive direction of the log([N II]/Hα) axis, and θ is the angle with respect to the positive direction of the log([O III]/Hβ) axis. Red points represent the projected polynomial dividing surface defined in 3D. Solid black lines represent our kinematic 1σ and 3σ demarcation lines, dashed lines are from Kewley et al. (2001), and dotted lines are from Kauffmann et al. (2003).

metal-rich clouds. Finally, the kinematic threshold separating regions dominated by different ionization mechanisms may simply not be constant, and a fixed proportion of contamination from spatially close AGN-ionized regions or DIG could translate into slightly different velocity dispersions for composite regions in galaxies with different stellar masses. The connection between the theoretically derived SF boundary and the empirically derived one presented here therefore cannot be easily understood without a consistent treatment of gas ionization properties and kinematics. Future work with sophisticated photoionization models based on hydrodynamical modeling of the gas structure might help to bridge the two methods.

8. Summary

We have presented the first large-scale IFU analysis of the distribution of ionized gas velocity dispersions in a representative sample of 9149 galaxies at median redshift $z = 0.04$. As we demonstrated in Section 3, velocity dispersion correlates strongly with the observed intensity ratios between strong nebular emission lines such as Hα, [O III], [N II], [S II], and [O I]. By virtue of this correlation, there exist well-defined regions in the multidimensional line ratio space for which the ionized gas is either dominated by a dynamically cold component with $\sigma_{\mathrm{H}\alpha} \approx 24 \pm 11\,\mathrm{km\,s^{-1}}$ or a dynamically warm component with a much broader distribution of $\sigma_{\mathrm{H}\alpha}$ extending up to $200\,\mathrm{km\,s^{-1}}$. The dynamically cold sequence corresponds closely to the regions covered by traditional stellar photoionization models, and we therefore identify it as representing star formation in H II regions embedded in galactic thin disks.

Given this strong correlation between the sources of the ionizing photons and the dynamical properties of the gas illuminated by these photons, we therefore used our observed isodispersion contours to construct a series of equations (Equations (1)–(6)) defining the 1σ and 3σ boundaries between star-forming spaxels and those dominated by AGN and/or LI(N)ER-like emission. While these new boundaries are rooted in the observed ionized gas velocity dispersion, we have demonstrated in Section 4 that they correspond closely to well-studied trends in other physical observables as well. The star-forming population has predominantly young ages and high star formation rates implied by the low D_n4000 and high Hα equivalent width, respectively, and ionized gas velocity dispersions that are 40% or less of the corresponding stellar velocity dispersion. In contrast, the LI(N)ER sequence is much older and has lower Hα equivalent width, with gas dispersions ~70% of the stellar velocity dispersion, consistent with expectations for a diffuse WIM. The AGN sequence in turn is intermediate in population age and Hα equivalent width but exhibits gas dispersions comparable to or in excess of the stellar velocity dispersion, indicative of radiative shocks and nonequilibrium gas flows. In practice the gas in each spaxel is by no means exclusively ionized by a single mechanism, and the Intermediate region between these sequences is therefore likely a combination of a traditional mixing sequence augmented by the rise in contributions from DIG in older stellar populations.

We explored the importance of selection effects to our conclusions in Section 5, the most crucial of which is the galactocentric radius of the spaxel sample. As we demonstrated in Section 5.4, there is a large population of low-metallicity rapidly star-forming spaxels at a distance of $1-2R_{\mathrm{eff}}$ in the MaNGA sample that is absent or severely underrepresented when we apply radial selection cuts designed to mimic the fiber aperture coverage of the original SDSS-I spectroscopic survey. These sample differences are almost entirely responsible for the offsets between our new dynamically defined sequences and the corresponding relations defined by Kewley et al. (2001) and Kauffmann et al. (2003).

We additionally provided theoretical support for our new classifications using updated photoionization models in Section 6; these updated models are capable of explaining the revised upper boundaries of both the [N II]/Hα and [S II]/Hα dynamically cold sequences. In contrast, the revised [O I]/Hα boundary cannot yet be explained theoretically, either

because of observational contamination from DIG or inadequacies in theoretical models.

Finally, we presented a multidimensional view of the diagnostic line ratio diagrams, noting how the folding of photoionization models in this space naturally leads to both an upper envelope of the star-forming sequence and artifacts when projected into two dimensions. For instance, the 3D surface defined by the $N2$, $S2$, and $R3$ line ratios exhibits a tail to the LI(N)ER sequence that (when projected into the $S2$ versus $R3$ space) manifests as a "bump" of old, high-$\sigma_{\mathrm{H}\alpha}$ spaxels below the traditional star-forming sequence. By allowing for a rotation of the projection angle of this 3D surface, we have determined a new two-dimensional projection that effectively minimizes such contamination (albeit comparably to the usual $N2-R3$ projection) and results in a strong and systematic gradient of $\sigma_{\mathrm{H}\alpha}$ across the projected line ratio space.

M.A.B. acknowledges NSF Awards AST-1517006 and AST-1814682.

Funding for the Sloan Digital Sky Survey IV has been provided by the Alfred P. Sloan Foundation, the US Department of Energy Office of Science, and the Participating Institutions. SDSS-IV acknowledges support and resources from the Center for High-Performance Computing at the University of Utah. The SDSS website is http://www.sdss.org.

SDSS-IV is managed by the Astrophysical Research Consortium for the Participating Institutions of the SDSS Collaboration including the Brazilian Participation Group, the Carnegie Institution for Science, Carnegie Mellon University, the Chilean Participation Group, the French Participation Group, Harvard-Smithsonian Center for Astrophysics, Instituto de Astrofísica de Canarias, The Johns Hopkins University, Kavli Institute for the Physics and Mathematics of the Universe (IPMU)/University of Tokyo, the Korean Participation Group, Lawrence Berkeley National Laboratory, Leibniz Institut für Astrophysik Potsdam (AIP), Max-Planck-Institut für Astronomie (MPIA Heidelberg), Max-Planck-Institut für Astrophysik (MPA Garching), Max-Planck-Institut für Extraterrestrische Physik (MPE), National Astronomical Observatories of China, New Mexico State University, New York University, University of Notre Dame, Observatário Nacional/MCTI, The Ohio State University, Pennsylvania State University, Shanghai Astronomical Observatory, United Kingdom Participation Group, Universidad Nacional Autónoma de México, University of Arizona, University of Colorado Boulder, University of Oxford, University of Portsmouth, University of Utah, University of Virginia, University of Washington, University of Wisconsin, Vanderbilt University, and Yale University.

ORCID iDs

David R. Law https://orcid.org/0000-0002-9402-186X
Xihan Ji https://orcid.org/0000-0002-1660-9502
Francesco Belfiore https://orcid.org/0000-0002-2545-5752
Matthew A. Bershady https://orcid.org/0000-0002-3131-4374
Michele Cappellari https://orcid.org/0000-0002-1283-8420
Kyle B. Westfall https://orcid.org/0000-0003-1809-6920
Renbin Yan https://orcid.org/0000-0003-1025-1711
Dmitry Bizyaev https://orcid.org/0000-0002-3601-133X
Joel R. Brownstein https://orcid.org/0000-0002-8725-1069
Niv Drory https://orcid.org/0000-0002-7339-3170
Brett H. Andrews https://orcid.org/0000-0001-8085-5890

References

Abolfathi, B., Aguado, D. S., Aguilar, G., et al. 2018, ApJS, 235, 42
Aguado, D. S., Ahumada, R., Almeida, A., et al. 2019, ApJS, 240, 23
Albareti, F. D., Allende Prieto, C., Almeida, A., et al. 2017, ApJS, 233, 25
Ali, B., Blum, R. D., Bumgardner, T. E., et al. 1991, PASP, 103, 1182
Allen, M. G., Groves, B. A., Dopita, M. A., et al. 2008, ApJS, 178, 20
Andersen, D. R., Bershady, M. A., Sparke, L. S., et al. 2006, ApJS, 166, 505
Badnell, N. R., Ferland, G. J., Gorczyca, T. W., et al. 2015, ApJ, 804, 100
Baldwin, J. A., Phillips, M. M., & Terlevich, R. 1981, PASP, 93, 5
Balogh, M. L., Morris, S. L., Yee, H. K. C., et al. 1999, ApJ, 527, 54
Belfiore, F., Maiolino, R., Maraston, C., et al. 2016, MNRAS, 461, 3111
Belfiore, F., Westfall, K. B., Schaefer, A., et al. 2019, AJ, 158, 160
Binette, L., Dopita, M. A., & Tuohy, I. R. 1985, ApJ, 297, 476
Binette, L., Magris, C. G., Stasińska, G., et al. 1994, A&A, 292, 13
Bizyaev, D., Walterbos, R. A. M., Yoachim, P., et al. 2017, ApJ, 839, 87
Blanton, M. R., Bershady, M. A., Abolfathi, B., et al. 2017, AJ, 154, 28
Blanton, M. R., Kazin, E., Muna, D., et al. 2011, AJ, 142, 31
Brinchmann, J., Charlot, S., White, S. D. M., et al. 2004, MNRAS, 351, 1151
Bundy, K., Bershady, M. A., Law, D. R., et al. 2015, ApJ, 798, 7
Burkert, A., Genzel, R., Bouché, N., et al. 2010, ApJ, 725, 2324
Byler, N., Dalcanton, J. J., Conroy, C., et al. 2017, ApJ, 840, 44
Byler, N., Dalcanton, J. J., Conroy, C., et al. 2019, AJ, 158, 2
Cappellari, M. 2017, MNRAS, 466, 798
Cappellari, M., & Copin, Y. 2003, MNRAS, 342, 345
Cappellari, M., Emsellem, E., Krajnović, D., et al. 2011, MNRAS, 413, 813
Cappellari, M., Scott, N., Alatalo, K., et al. 2013, MNRAS, 432, 1709
Chabrier, G. 2003, PASP, 115, 763
Cherinka, B., Andrews, B. H., Sánchez-Gallego, J., et al. 2019, AJ, 158, 74
Choi, J., Dotter, A., Conroy, C., et al. 2016, ApJ, 823, 102
Cid Fernandes, R., Stasińska, G., Schlickmann, M. S., et al. 2010, MNRAS, 403, 1036
Conroy, C., Gunn, J. E., & White, M. 2009, ApJ, 699, 486
Croom, S. M., Lawrence, J. S., Bland-Hawthorn, J., et al. 2012, MNRAS, 421, 872
D'Agostino, J. J., Kewley, L. J., Groves, B. A., et al. 2019, MNRAS, 487, 4153
Davies, R. L., Groves, B., Kewley, L. J., et al. 2016, MNRAS, 462, 1616
Dekel, A., Birnboim, Y., Engel, G., et al. 2009, Natur, 457, 451
Della Bruna, L., Adamo, A., Bik, A., et al. 2020, A&A, 635, A134
den Brok, M., Carollo, C. M., Erroz-Ferrer, S., et al. 2020, MNRAS, 491, 4089
Domgorgen, H., & Mathis, J. S. 1994, ApJ, 428, 647
Dopita, M. A. 1995, Ap&SS, 233, 215
Dopita, M. A., Kewley, L. J., Heisler, C. A., et al. 2000, ApJ, 542, 224
Dopita, M. A., Kewley, L. J., Sutherland, R. S., et al. 2016, Ap&SS, 361, 61
Dopita, M. A., Sutherland, R. S., Nicholls, D. C., et al. 2013, ApJS, 208, 10
Dotter, A. 2016, ApJS, 222, 8
Drory, N., MacDonald, N., Bershady, M. A., et al. 2015, AJ, 149, 77
Erb, D. K., Shapley, A. E., Pettini, M., et al. 2006, ApJ, 644, 813
Ferland, G. J., Chatzikos, M., Guzmán, F., et al. 2017, RMxAA, 53, 385
Ferland, G. J., Porter, R. L., van Hoof, P. A. M., et al. 2013, RMxAA, 49, 137
Fioc, M., & Rocca-Volmerange, B. 1997, A&A, 500, 507
Flores-Fajardo, N., Morisset, C., Stasińska, G., et al. 2011, MNRAS, 415, 2182
Förster Schreiber, N. M., Renzini, A., Mancini, C., et al. 2018, ApJS, 238, 21
García-Marín, M., Colina, L., Arribas, S., et al. 2006, ApJ, 650, 850
García-Marín, M., Colina, L., Arribas, S., et al. 2009, A&A, 505, 1319
Green, A. W., Glazebrook, K., McGregor, P. J., et al. 2014, MNRAS, 437, 1070
Groves, B. A., Dopita, M. A., & Sutherland, R. S. 2004, ApJS, 153, 9
Gu, M., Conroy, C., Law, D., et al. 2018, ApJ, 859, 37
Gunn, J. E., Siegmund, W. A., Mannery, E. J., et al. 2006, AJ, 131, 2332
Heckman, T. M. 1980, A&A, 500, 187
Hillier, D. J., & Miller, D. L. 1998, ApJ, 496, 407
Ho, I.-T., Kewley, L. J., Dopita, M. A., et al. 2014, MNRAS, 444, 3894
Ho, L. C., Filippenko, A. V., & Sargent, W. L. W. 1997, ApJS, 112, 315
Ilha, G. S., Riffel, R. A., Schimoia, J. S., et al. 2019, MNRAS, 484, 252
Ji, X., & Yan, R. 2020, MNRAS, 499, 5749
Jimenez-Vicente, J., Battaner, E., Rozas, M., Castaneda, H., & Porcel, C. 1999, A&A, 342, 417
Kauffmann, G., Heckman, T. M., Tremonti, C., et al. 2003, MNRAS, 346, 1055
Kewley, L. J., & Dopita, M. A. 2002, ApJS, 142, 35
Kewley, L. J., Dopita, M. A., Leitherer, C., et al. 2013, ApJ, 774, 100
Kewley, L. J., Dopita, M. A., Sutherland, R. S., et al. 2001, ApJ, 556, 121
Kewley, L. J., Groves, B., Kauffmann, G., et al. 2006, MNRAS, 372, 961
Kewley, L. J., Nicholls, D. C., & Sutherland, R. S. 2019, ARA&A, 57, 511

Krumholz, M. R., Burkhart, B., Forbes, J. C., et al. 2018, MNRAS, 477, 2716
Lacerda, E. A. D., Cid Fernandes, R., Couto, G. S., et al. 2018, MNRAS, 474, 3727
Law, D. R., Cherinka, B., Yan, R., et al. 2016, AJ, 152, 83
Law, D. R., Steidel, C. C., Erb, D. K., et al. 2009, ApJ, 697, 2057
Law, D. R., Westfall, K. B., Bershady, M. A., et al. 2021, AJ, 161, 52
Law, D. R., Yan, R., Bershady, M. A., et al. 2015, AJ, 150, 19
Leitherer, C., Schaerer, D., Goldader, J. D., et al. 1999, ApJS, 123, 3
Levesque, E. M., Kewley, L. J., & Larson, K. L. 2010, AJ, 139, 712
Levy, R. C., Bolatto, A. D., Sánchez, S. F., et al. 2019, ApJ, 882, 84
López-Cobá, C., Sánchez, S. F., Anderson, J. P., et al. 2020, AJ, 159, 167
Maiolino, R., & Mannucci, F. 2019, A&ARv, 27, 3
Maiolino, R., Nagao, T., Grazian, A., et al. 2008, A&A, 488, 463
Maraston, C., Hill, L., Thomas, D., et al. 2020, MNRAS, 496, 2962
Marigo, P., Girardi, L., Bressan, A., et al. 2008, A&A, 482, 883
Mathis, J. S. 1986, ApJ, 301, 423
Mingozzi, M., Belfiore, F., Cresci, G., et al. 2020, A&A, 636, A42
Monreal-Ibero, A., Arribas, S., & Colina, L. 2006, ApJ, 637, 138
Monreal-Ibero, A., Arribas, S., Colina, L., et al. 2010, A&A, 517, A28
Noll, S., Burgarella, D., Giovannoli, E., et al. 2009, A&A, 507, 1793
Oparin, D. V., & Moiseev, A. V. 2018, AstBu, 73, 298
Osterbrock, D. E. 1989, Astrophysics of Gaseous Nebulae and Galactic Nuclei (Mill Valley, CA: Univ. Science Books)
Pauldrach, A. W. A., Hoffmann, T. L., & Lennon, M. 2001, A&A, 375, 161
Péroux, C., & Howk, J. C. 2020, ARA&A, 58, 363
Pettini, M., & Pagel, B. E. J. 2004, MNRAS, 348, L59
Relano, M., Beckman, J. E., Zurita, A., Rozas, M., & Giammanco, C. 2005, A&A, 431, 235
Reynolds, R. J. 1990, ApJL, 349, L17
Rich, J. A., Kewley, L. J., & Dopita, M. A. 2011, ApJ, 734, 87
Rousseeuw, P. J., & van Driessen, K. 2006, Data Min. Knowl. Disc., 12, 29
Rozas, M., Relano, M., Zurita, A., & Beckman, J. E. 2002, A&A, 386, 42
Rozas, M., Zurita, A., Beckman, J. E., & Perez, D. 2000, A&AS, 142, 259
Sánchez, S. F. 2020, ARA&A, 58, 99
Sánchez, S. F., Kennicutt, R. C., Gil de Paz, A., et al. 2012a, A&A, 538, A8
Sánchez, S. F., Rosales-Ortega, F. F., Iglesias-Páramo, J., et al. 2014, A&A, 563, A49
Sánchez, S. F., Rosales-Ortega, F. F., Marino, R. A., et al. 2012b, A&A, 546, A2
Sánchez, S. F., Walcher, C. J., Lopez-Coba, C., et al. 2021, RMxAA, 57, 3
Sanders, R. L., Shapley, A. E., Jones, T., et al. 2021, ApJ, 914, 19
Sarzi, M., Shields, J. C., Schawinski, K., et al. 2010, MNRAS, 402, 2187
Singh, R., van de Ven, G., Jahnke, K., et al. 2013, A&A, 558, A43
Smee, S. A., Gunn, J. E., Uomoto, A., et al. 2013, AJ, 146, 32
Smith, L. J., Norris, R. P. F., & Crowther, P. A. 2002, MNRAS, 337, 1309
Stasińska, G., Cid Fernandes, R., Mateus, A., et al. 2006, MNRAS, 371, 972
Steidel, C. C., Strom, A. L., Pettini, M., et al. 2016, ApJ, 826, 159
Strom, A. L., Steidel, C. C., Rudie, G. C., et al. 2017, ApJ, 836, 164
Sutherland, R. S., & Dopita, M. A. 1993, ApJS, 88, 253
Topping, M. W., Shapley, A. E., Reddy, N. A., et al. 2020, MNRAS, 495, 4430
Tremonti, C. A., Heckman, T. M., Kauffmann, G., et al. 2004, ApJ, 613, 898
Tumlinson, J., Peeples, M. S., & Werk, J. K. 2017, ARA&A, 55, 389
Varidel, M. R., Croom, S. M., Lewis, G. F., et al. 2020, MNRAS, 495, 2265
Veilleux, S., & Osterbrock, D. E. 1987, ApJS, 63, 295
Vogt, F. P. A., Dopita, M. A., Kewley, L. J., et al. 2014, ApJ, 793, 127
Wake, D. A., Bundy, K., Diamond-Stanic, A. M., et al. 2017, AJ, 154, 86
Weigel, A. K., Schawinski, K., & Bruderer, C. 2016, MNRAS, 459, 2150
Westfall, K. B., Cappellari, M., Bershady, M. A., et al. 2019, AJ, 158, 231
Yan, R., & Blanton, M. R. 2012, ApJ, 747, 61
Yan, R., Bundy, K., Law, D. R., et al. 2016, AJ, 152, 197
Yan, R., Chen, Y., Lazarz, D., et al. 2019, ApJ, 883, 175
Yan, R., Newman, J. A., Faber, S. M., et al. 2006, ApJ, 648, 281
Yan, R., Tremonti, C., Bershady, M. A., et al. 2016, AJ, 151, 8
Zhang, K., & Hao, L. 2018, ApJ, 856, 171
Zhang, K., Yan, R., Bundy, K., et al. 2017, MNRAS, 466, 3217